

EFFECTS OF MAGNESIUM REDUCTION ON THE STRUCTURE AND
ELECTRICAL PROPERTIES OF TANTALUM OXIDE AEROGELS

by

Lupita Sarahi Aguirre, B.S.

A thesis submitted to the Graduate Council of
Texas State University in partial fulfillment
of the requirements for the degree of
Master of Science
with a Major in Chemistry
August 2020

Committee Members:

Christopher P. Rhodes, Chair

Benjamin Martin

Shane Yost

COPYRIGHT

by

Lupita Sarahi Aguirre

2020

FAIR USE AND AUTHOR'S PERMISSION STATEMENT

Fair Use

This work is protected by the Copyright Laws of the United States (Public Law 94-553, section 107). Consistent with fair use as defined in the Copyright Laws, brief quotations from this material are allowed with proper acknowledgement. Use of this material for financial gain without the author's express written permission is not allowed.

Duplication Permission

As the copyright holder of this work I, Lupita Sarahi Aguirre, authorize duplication of this work, in whole or in part, for educational or scholarly purposes only.

DEDICATION

I dedicate this work to my dear Lord Jesus Christ, the potter, who has authority over the clay to make out of the same lump one vessel unto honor and another unto dishonor. To You who will make known the riches of His glory upon vessels of mercy, which He had before prepared unto glory.

To my beloved husband, mi Juanito, who has been faithful to our commitment in spite of the outward situation. Thank you for supporting me, guiding me, and walking with me during this journey. Te amo!

To my mom, Nereida, who has always been a source of supply and whose person reminds me that my source is not weak, but strong, since she is a woman who has trusted in Jehovah and whose trust Jehovah is. Gracias mami!

To my family especially my brothers, Samuel and Vicente, who always believe in me. Thank you for encouraging me, protecting me, and for loving me unconditionally. To Janet, Erandi, Victoria, Samantha y Melissa, thank you for bringing joy to my life. To my father, Vicente, thank you for your faithful advice.

To the brothers and sisters in the church in San Marcos and Austin, thank you for shepherding me before, during, and after my time as a graduate student at Texas State University. I am thankful to know that I am not running the race on my own but with each and every one of you.

ACKNOWLEDGEMENTS

I would like to acknowledge funding from the Office of Naval Research (Grant number N00014-19-1-2071) and The Graduate College at Texas State University (Thesis Research Support Fellowship, Fall 2019) for support of this research.

I would like to recognize Dr. Christopher P. Rhodes, Dr. Fernando Godinez Salomon, and Jesus Adame Solorio who significantly contributed and faithfully helped during the entire research project.

I would like to thank my thesis committee members, Dr. Benjamin Martin and Dr. Shane Yost, for their instruction and training during the research project.

Most of all, I would like to express my sincere gratitude to my research advisor, Dr. Christopher P. Rhodes, for the opportunity to return to the scientific field as part of his research group, for his personal supervision, and for access to his research laboratory. Dr. Rhodes, you have been a role model of both professional excellence and outstanding character. Thank you for encouraging me to persevere in my research project, supporting my academic development at Texas State University, and helping me achieve my professional goals. Thank you so much Dr. Rhodes!

TABLE OF CONTENTS

	Page
ACKNOWLEDGEMENTS	v
LIST OF TABLES	viii
LIST OF FIGURES	ix
LIST OF ABBREVIATIONS.....	xi
ABSTRACT.....	xii
CHAPTER	
1. INTRODUCTION	1
1.1. Background and Overview of Proton Exchange Membrane Fuel Cells	1
1.2 Characteristics of Support Materials.....	5
1.3 Metal Oxides as Alternative Support Materials.....	7
1.4 Sol-gel Synthesis Method (High Surface Area and Porous Materials)	11
1.5 Magnesium Reduction (Enhanced Electronic Conductivity)	14
1.6 Project Motivation and Objectives.....	17
2. MATERIALS AND METHODS.....	19
2.1 Chemicals.....	19
2.2 Synthesis of Tantalum Oxide Gels	19
2.3 Thermal Treatments	20
2.4 Magnesium Reduction Method.....	20
2.5 Chemical Leaching	20
2.6 Sample Notations	21
2.7 Physical and Structural Characterization	21
2.8 Electronic Measurements.....	22
3. RESULTS AND DISCUSSION	24

3.1 Effect of Thermal Treatment in the Crystal Structure of TaO _x Aerogels	24
3.2 Effect of Mg Reduction in TaO _x Aerogels Physical Properties.....	26
3.3 Effect of Mg Reduction on The Morphology of TaO _x Aerogels	28
3.4 Effect of Mg Reduction on The Chemical Composition of TaO _x Aerogels	30
3.5 Effect of Mg Reduction in The Crystal Structure of TaO _x Aerogels	32
3.6 Analysis on The Degree of Reduction in TaO _x Aerogels	35
3.7 Analysis of Oxygen Concentration.....	37
3.8 Comparison of The Composition from EDS and XRD Analysis	42
3.9 Analysis of Surface Area and Porosity	43
3.10 Evaluation of The Electronic Conductivity	45
4. CONCLUSIONS.....	49
BIBLIOGRAPHY.....	51

LIST OF TABLES

Table	Page
1. Change in electrochemical surface area (ECSA) for noble metal supported on carbon vs. noble metal supported on supports containing TaO _x	11
2. Metal oxide aerogels (surface area and pore size).	14
3. Notation used to label different TaO _x aerogels.	21
4. Atomic ratio determined from Energy Dispersive X-ray Spectroscopy (EDS) analysis of TaO _x aerogels.	32
5. Degree of reduction based on standard references of XRD patterns.	36
6. X-ray diffraction parameters of Ta-Ap-Mg-CL and Ta-850-Mg-CL.	37
7. Composition of TaO _x aerogels from Energy Dispersive X-ray Spectroscopy (EDS) and X-ray Diffraction (XRD) analysis.	42
8. N ₂ Physisorption surface area, cumulative pore volume, and mean pore diameter of materials: Ta-Ap, Ta-Ap-Mg-CL, and Ta-850-Mg-CL.	44
9. Electronic conductivity of Ta-Ap, Ta-Ap-Mg-CL, and Ta-850-Mg-CL.	45

LISTS OF FIGURES

Figure	Page
1. U.S. energy consumption by energy source, 2018.....	1
2. Schematic representation of a Proton Exchange Membrane Fuel Cell (PEMFC) illustrating the anode, electrolyte, cathode, and the flow of electrons.....	2
3. A schematic diagram of the startup/shutdown operation mode.....	4
4. Simplified representation of suggested degradation mechanisms for platinum particles on a carbon support in fuel cells.....	5
5. A model of a supported metal particle, illustrating the effects of strong metal support interactions when Pt particles are supported on Ta ₂ O ₅	8
6. Dissolution potentials (U_{diss}) as a function of the number of Pt (111) layers on the metal oxide supports	9
7. Pourbaix Diagram of Tantalum and Ta ₂ O ₅	10
8. Schematic representation of the sol-gel method.....	12
9. Three different drying techniques of a wet gel	13
10. Ellingham diagram.....	16
11. Stainless steel electrodes (gray) with the material introduced in between the two electrodes (black).....	23
12. Schematic diagram of the conductivity cell made in-house of two stainless steel electrodes, insulating rings, and the pressed material in between the electrodes to obtain two-point probe measurements.....	23
13. Thermogravimetric Analysis (TGA) curve of TaO _x xerogel.....	24
14. X-ray diffraction (XRD) of TaO _x aerogels obtained at different temperatures (as-prepared, 550°C, and 850°C); diffraction peaks corresponding to monoclinic Ta ₂ O ₅ reference (00-019-1298) are shown at the bottom of the figure	26

15. (a-c) Pictures of the Mg reduction steps performed to the as-prepared TaO _x aerogel; (d-f) pictures of the Mg reduction steps performed to the 850-thermally treated TaO _x aerogel; (g) schematic illustration of the Mg reduction steps.....	27
16. (a-c) Scanning Electron Microscopy (SEM) pictures of the Mg reduction steps performed to the as-prepared TaO _x aerogel; (d-f) pictures of the Mg reduction steps performed to the 850-thermally treated TaO _x aerogel	30
17. Scanning electron microscopy (SEM) images of (a) Ta-Ap, (g) Ta-Ap-Mg-CL, (m) Ta-850, and (s) Ta-850-Mg-CL; element map composition of tantalum (b, h, n, t), oxygen (c, i, o, and u), magnesium (d, j, p, and v), carbon (e, k, q, and w), and chlorine (f, l, r, and x).	31
18. X-ray diffraction (XRD) patterns of as-prepared TaO _x aerogel (Ta-Ap), Ta-Ap after Mg reduction (Ta-Ap-Mg), and Ta-Ap-Mg after chemical leaching (Ta-Ap-Mg-CL); diffraction peaks corresponding to standard references for TaO, MgO, metallic Ta, and Ta ₂ O are shown at the bottom of the figure.....	34
19. X-ray diffraction (XRD) patterns of 850-thermally treated TaO _x aerogel (Ta-850), Ta-850 after Mg reduction (Ta-850-Mg), and Ta-850-Mg after chemical leaching (Ta-850-Mg-CL); diffraction peaks corresponding to the dark blue, gray, red, and light blue vertical lines at the bottom represent the diffraction patterns of Ta ₂ O, metallic Ta, MgO, and monoclinic Ta ₂ O ₅ respectively	35
20. Average 2θ values for the (111) peak on TaO standard (gray), Ta-Ap-Mg (green), and Ta-Ap-Mg-CL (blue); average 2θ values for the (220) peak of Ta ₂ O standard (gray), Ta-850-Mg (green), and Ta-850-Mg-CL (blue).....	38
21. Linear extrapolation of the oxygen content in metallic Ta standard reference, TaO standard reference, and Ta-Ap-Mg-CL aerogel sample	40
22. Linear extrapolation of the oxygen content in metallic Ta standard reference, Ta ₂ O standard reference, and Ta-850-Mg-CL aerogel sample.....	41
23. Pore size distribution of the as-prepared TaO _x aerogel (gray), Ta-Ap-Mg-CL (green), Ta-850-Mg-CL (blue).....	44

LIST OF ABBREVIATIONS

Abbreviation	Description
PEMFC	Proton Exchange Membrane Fuel Cell
ORR	Oxygen reduction reaction
SMSI	Strong metal–support interaction
U_{diss}	Dissolution potential of platinum
ECSA	Electrochemical surface area
XRD	X-ray Diffraction
COD	Crystallography open database
BET	Brunauer– Emmett–Teller
BJH	Barrett–Joyner–Halenda
SEM	Scanning electron microscopy
EDS	Energy dispersive X-ray spectroscopy
TGA	Thermogravimetric analysis

ABSTRACT

Electrocatalyst supports that have resistance to corrosion, high surface area, high porosity, and adequate electronic conductivity are needed to improve the durability of proton-exchange membrane fuel cells (PEMFC) utilized for transportation, stationary, and portable power applications. Although platinum supported on carbon is the typical electrocatalyst used for the oxygen reduction reaction (ORR) in PEMFCs, the corrosion of carbon presents a challenge for the widespread and commercialization of this technology. Tantalum pentoxide (Ta_2O_5) is stable under the oxidative potentials and acidic conditions of the ORR, but prior efforts have largely focused on carbon- Ta_2O_5 -Pt catalysts which can still result in the degradation of the support. To develop a potential Ta_2O_5 support, the effects of thermal treatments and magnesium reduction of tantalum oxide aerogels were evaluated in order to create a support material that meets the required characteristics typically observed in carbon-based supports. Sol-gel synthesis and supercritical drying were performed to obtain tantalum oxide (TaO_x) aerogels with high surface area and porosity. Thermal treatments in air and thermal reduction using magnesium (Mg) as a reducing agent were investigated to improve the crystallinity and electronic conductivity of TaO_x aerogels. The morphology and structure of TaO_x aerogels were determined using scanning electron microscopy, nitrogen physisorption, and X-ray diffraction measurements. Electronic conductivity measurements were obtained using a two-point probe configuration. Results indicated that the sol-gel synthesis method was a viable approach to produce TaO_x aerogels with high surface areas of $197 \text{ m}^2\text{g}^{-1}$ and mean

pore diameters of 11 nm. Subsequent thermal treatments in air and Mg reduction modified the crystal structure, reduced the oxygen content, and improved the electronic conductivity of TaO_x aerogels. Mg reduction of the as-prepared TaO_x aerogel produced a material with a TaO crystal structure, a surface area of 54 m²g⁻¹, and an electronic conductivity of 3.7x10⁻³ S cm⁻¹. Moreover, Mg reduction on the 850°C-thermally treated TaO_x aerogel produced a material with Ta₂O crystal structure, a surface area of 11 m²g⁻¹, and an electronic conductivity of 3.5x10⁻⁴ S cm⁻¹. From this study, sol-gel synthesis, thermal treatments, and Mg reduction were shown to improve the resulting structure, morphology, and electronic conductivity of TaO_x aerogels making them potential alternatives to replace carbon-based supports. Understanding the effect of thermal treatments and Mg reduction in TaO_x aerogels opens up new opportunities for the design and development of highly durable and stable carbon-free ORR electrocatalyst supports for fuel cells.

1. INTRODUCTION

1.1 Background and Overview of Proton Exchange Membrane Fuel Cells

Fossil fuels including oil (petroleum), natural gas, and coal are a primary source of energy that is widely used in many different countries for energy production. Fossil fuels are not a renewable energy source as they cannot be produced at the same rate at which they are being consumed.¹ However, petroleum remains as the major transportation fuel of choice because of its energy content, easy transportability, and reasonable availability.² In 2018, fossil fuels accounted for ~ 80% of the total U.S. energy consumption while renewable energy only accounted for ~11% (Figure 1).³

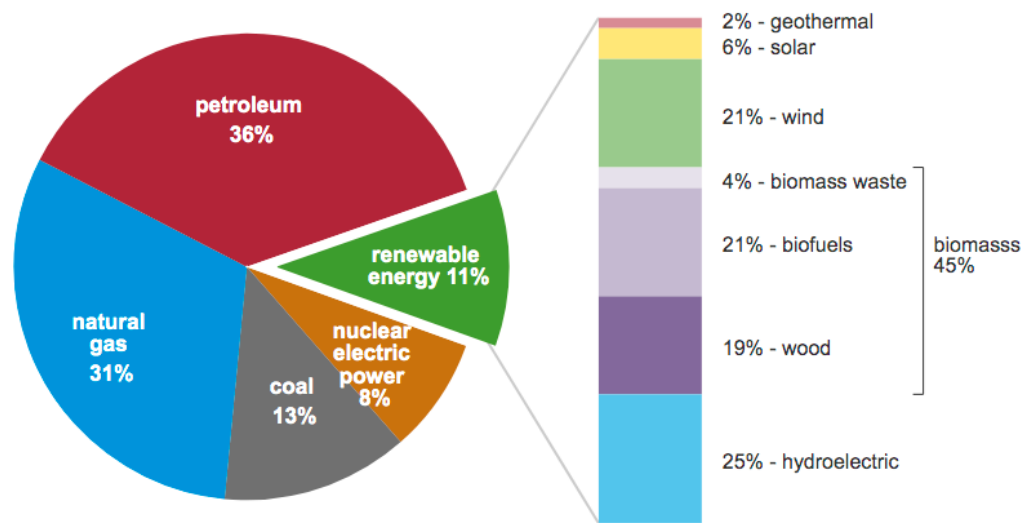


Figure 1. U.S. energy consumption by energy source, 2018.³

The use of fossil fuels as a primary source of energy is not sustainable for the long run since their combustion is a major contribution of carbon dioxide, a major factor to the earth's pollution and climate change.² As a result, significant progress has been made in the advancement of hydrogen-based renewable technologies for the automobile sector.

Fuel cells are energy conversion devices that generate electricity from an electrochemical reaction in which oxygen and hydrogen-rich fuel combine to form water.⁴ There are different types of fuel cells and their classification depends upon the type of fuel, electrolyte, and temperature of operation.⁵ Proton Exchange Membrane Fuel Cells (PEMFC) use hydrogen or ethanol as their fuel source, perfluorosulfonic acid or hydrocarbon-based membrane as the electrolyte, and normally operate between 0°C to 95°C.^{2, 6} The typical components of a PEMFC consist of a negative electrode (anode) and a positive electrode (cathode) separated by an ion-conducting electrolyte (Figure 2).

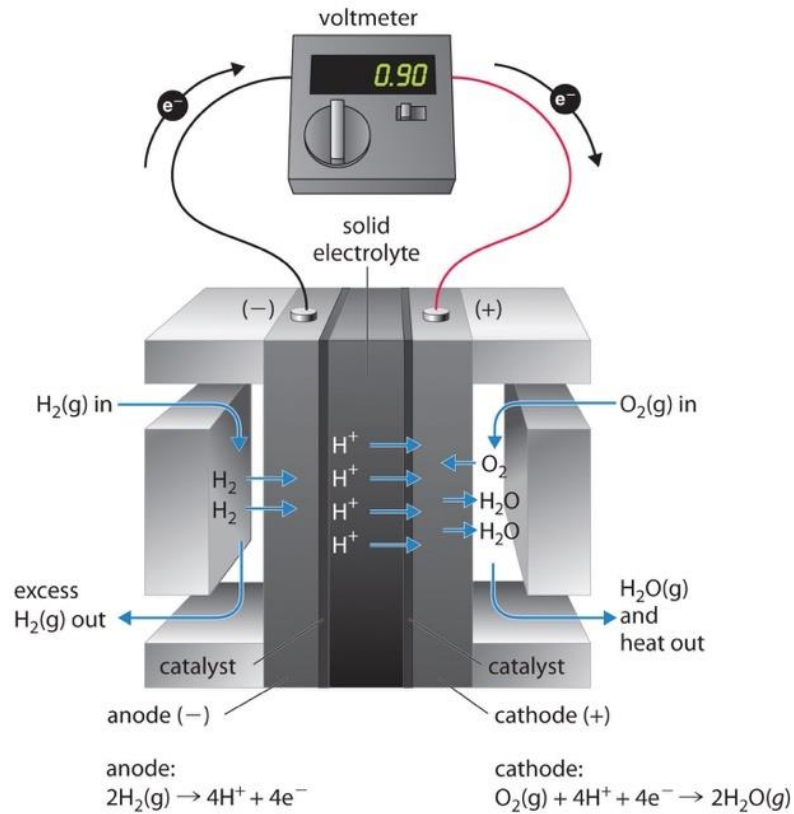


Figure 2. Schematic representation of a Proton Exchange Membrane Fuel Cell (PEMFC) illustrating the anode, electrolyte, cathode, and the flow of electrons.²

At the anode, hydrogen atoms that serve as the fuel source, are separated into protons (H⁺) and electrons (e⁻), as described by the following equation.



The generated electrons travel through an external circuit, generating electricity and ultimately powering the device connected to the fuel cell.² The protons that were generated at the anode side migrate through the electrolyte to the cathode side where they react with oxygen and electrons to produce water and heat according to the following equation.



The overall reaction is observed in Equation 3.



The use of a catalyst is crucial at the anode for the activation energy barrier to be overcome and for the hydrogen oxidation reaction to be kinetically feasible at $< 80 \text{ }^\circ\text{C}$ (Equation 1). At the cathode, the use of a catalyst is also necessary to perform the kinetically slow 4e^- transfer during the oxygen reduction reaction (Equation 2).^{2, 7} Currently, platinum supported on carbon black is the state-of-the-art catalyst used in both electrodes. However, the startup/shutdown operation mode is a major concern for the degradation of the components of the fuel cell.⁸ When a fuel cell has been shut down for a period of time, it will be filled with air that has leaked from the environment in both the anode and the cathode compartments. On starting up the vehicle, hydrogen is injected into the anode resulting in a hydrogen-air front passing through the anode, leading to extremely high potentials at the cathode. Potentials of 1.5 V at the cathode are high enough to cause carbon corrosion and severe irreversible degradation of the electrocatalyst (Figure 3). The carbon corrosion reaction in aqueous solutions can be

thermodynamically oxidized at potentials above 0.207 V,⁹ and it is described by the following equation.

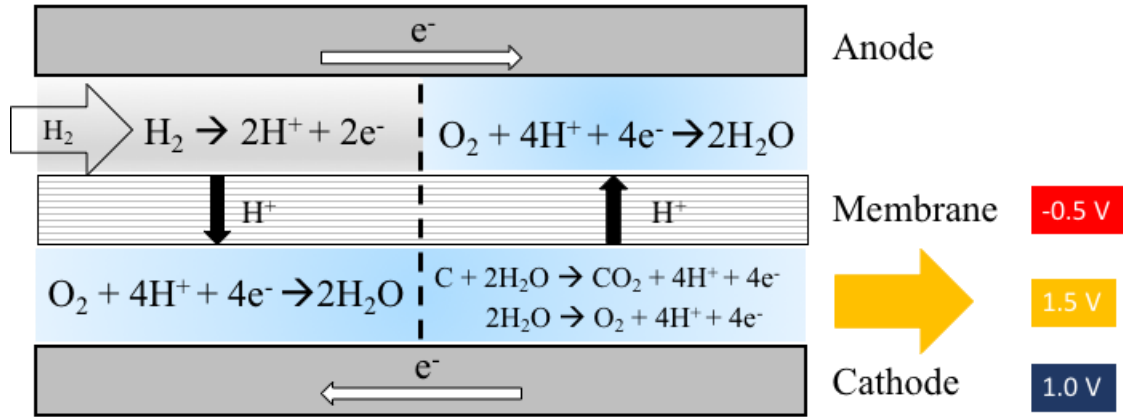


Figure 3. A schematic diagram of the startup/shutdown operation mode. A high potential of 1.5 V at the cathode catalyst layer leads to catastrophic degradation in a short period of time.²

Different operational modes can lead to Pt dissolution since Pt thermodynamically dissolves at ~ 1.18 V at 80°C .² The dissolution of Pt will enhance the formation of Pt band deposits in the membrane of the fuel cell, ultimately leading to system degradation.¹⁰ Figure 4 illustrates the different degradation processes that can occur in PEMFCs. Carbon corrosion and Pt dissolution are considered primary degradation processes and also contribute to secondary degradation processes such as particle detachment, agglomeration, and Ostwald ripening.¹¹

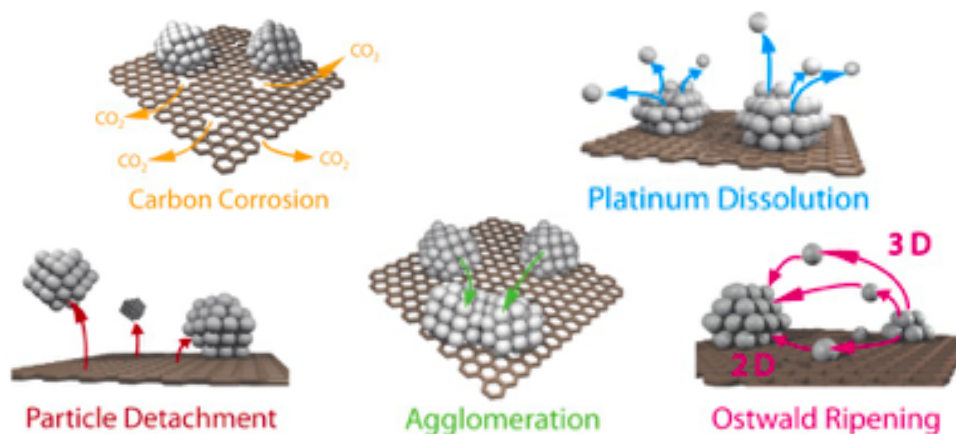


Figure 4. Simplified representation of suggested degradation mechanisms for platinum particles on a carbon support in fuel cells.¹¹

Particle detachment occurs due to the weakening of the interaction between platinum particles and the carbon support. A possible explanation of particle agglomeration is that neighboring platinum particles may come into contact with each other due to the shrinkage of the carbon support. Ostwald ripening happens when the dissolved platinum particles are redeposited on other large platinum particles resulting in significant particle growth. Overall, carbon corrosion causes the loss of the structural integrity of the catalyst layer leading to a decrease in porosity, mass transport limitations, and ultimately overall loss in fuel cell's performance.¹¹

1.2 Characteristics of Support Materials

For the long-term operation of PEMFC, it is important to find corrosion-resistant support materials that meet or improve the characteristics of carbon-based supports. Carbon supports have: (i) high surface areas (ca. 100-1,000 m²g⁻¹), (ii) high porosity, and (iii) high electronic conductivity (ca. 1-10 S/cm).⁹ Thus, before developing an alternative

viable carbon-free support, it is important to understand the unique properties required in an electrocatalyst support and the role each one of them plays in PEMFCs.

High surface area allows for a finer dispersion of Pt particles resulting in a high utilization of Pt metal on the support.¹² Uchida et al. observed that the increase in surface area of the support from 58 to 1500 m²g⁻¹ resulted in Pt particle size reduction from 3.7 to 1.0 nm.¹³ Increasing the surface area is an excellent approach to decrease Pt loadings and subsequently PEMFC cost.

Furthermore, high porosity in a support material favors the efficient mass transfer of liquids and gases, diminishes water flooding in the electrodes, and increases the interaction among neighboring molecules. Adequate mass transfer of liquids and gases requires that the transport paths, through which the molecules move into or out of the catalytic active sites, be open and porous for the molecules to travel easily and for the reactions to occur most effectively.¹⁴ To avoid flooding problems at the site of the cathode catalyst layer at high current densities, a catalyst support should possess a very small amount of micropore volume (< 2 nm), large portion of mesopores (2-50 nm), and a few macropores (> 50 nm).¹⁵ Lastly, a prior study indicated that for a large molecular catalyst such as iron corrole, a certain pore size (20 nm) in the carbon support enabled the catalytic molecules to be near each other.¹⁶ As a result, there was a greater electronic interaction among the iron corroles leading to higher catalytic activities during ORR.

Additionally, adequate electronic conductivity on the support is necessary to allow for the proper electron transport from the support to the noble metal catalyst. Support materials that have good conductivity allow the transfer of electrons leading to a higher activity of the catalysts.¹² A prior study indicated that the higher resistance for

charge transport on the support correlated with the increase of voltage needed to obtain a given increment of current.¹⁷

Lastly, resistance to corrosion is an important feature for support materials to possess. When a support material is electrochemically stable in acidic media under the working conditions of PEMFC, it will prevent the degradation processes that can occur in an electrocatalyst (support corrosion, platinum dissolution, particle detachment, agglomeration, and Ostwald ripening). Since corrosion of the support weakens the interaction between the catalyst and the support material, it is crucial to develop support materials that are resistant to corrosion in order to prevent degradation of the fuel cell components and maintain a high catalytic performance.¹¹⁻¹² Although it is challenging to meet all the required characteristics of typical carbon-based supports simultaneously, the design of new synthesis procedures and the understanding of the fundamental properties of alternative materials can open up new opportunities for the development of carbon-free supports with adequate physicochemical properties for the application of fuel cells and other important electrochemical energy devices.

1.3 Metal Oxides as Alternative Support Materials

In recent years, metal oxides have been regarded as potential materials to replace carbon-based supports because of their high resistance to corrosion in an electrochemical environment, low dissolution in acidic media, and adequate stability against electrochemical corrosion presented in PEMFCs.¹² Furthermore, it has been observed that when Pt particles are tightly bound to metal oxide supports, Pt particles are protected from the different degradation process typically observed in carbon-based supports.¹⁸⁻²⁰

Prior studies have attributed the stabilization of Pt nanoparticles on metal oxide supports to the presence of strong metal support interactions (SMSI) between platinum particles and the metal oxide (Figure 5).²¹⁻²²

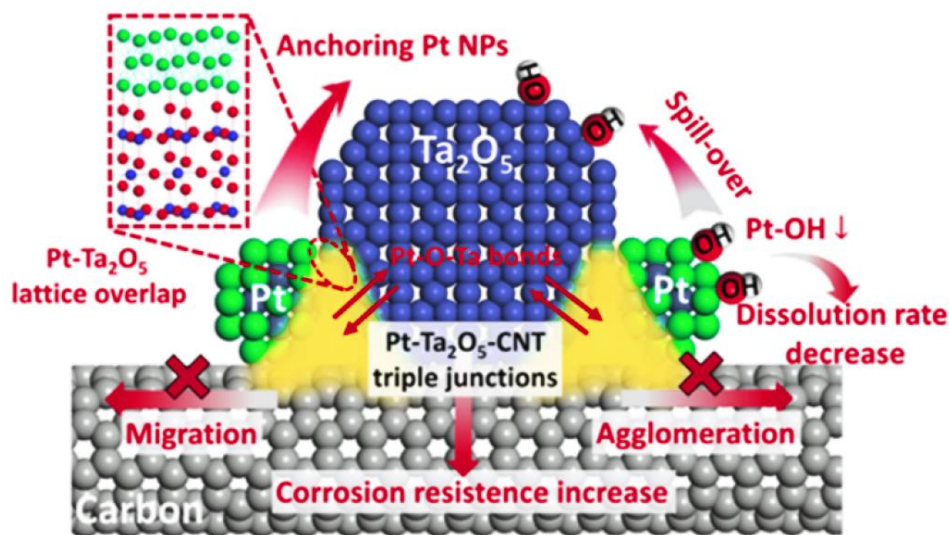


Figure 5. A model of a supported metal particle, illustrating the effects of strong metal support interactions when Pt particles are supported on Ta₂O₅.²²

Thermochemical calculations of Sn, Ti, Nb, Sb, W, and Ta, concluded that their metal oxides, hydroxides, or metals were among the most stable materials at 80 °C in strong acidic (pH=0) environments typical of PEMFC cathode conditions.²³ Although titanium oxide (TiO_x) has been the most widely studied and frequently used metal oxide catalyst support for ORR in PEMFC,^{20, 24-26} a recent report by General Motors Company indicated the necessity to avoid TiO_x as catalyst support because it can lead to significant degradation of the polymeric membrane, causing membrane thinning, and increased gas crossover.²⁷ In addition, when the activity and stability of overlayers of Pt supported on different metal oxides (Ti, Sn, Ta, Nb, Hf, and Zr) were analyzed, the dissolution potential (U_{diss}) of Pt went beyond 1.2 V when Pt particles were supported on TaO₂ rather

than TiO_2 (Figure 6).²⁸ Values lower than 1.2 V favored sintering of Pt particles, but values greater 1.2 V indicated a shift in the U_{diss} of Pt beyond 1.2 V as a result of the strong binding between Pt particles and the metal oxide.

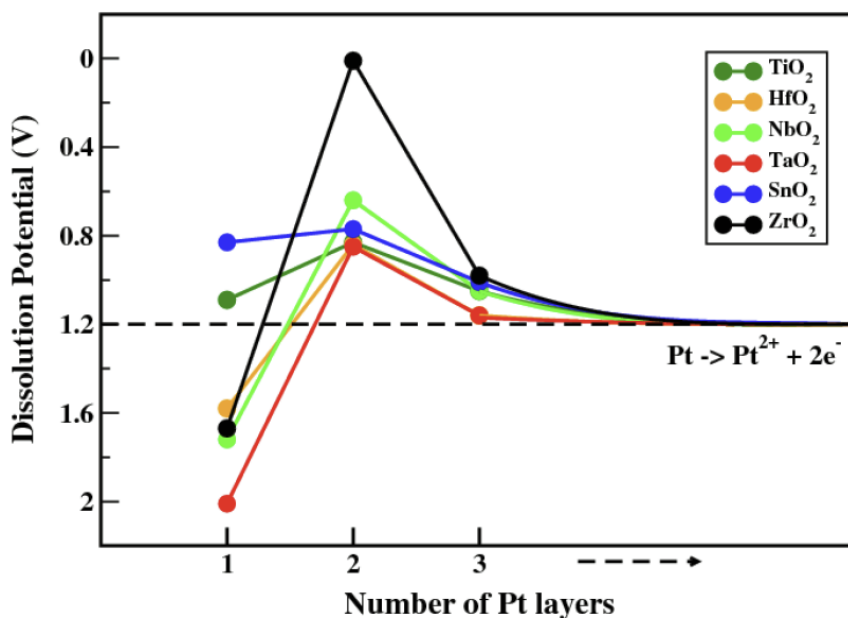


Figure 6. Dissolution potentials (U_{diss}) as a function of the number of Pt (111) layers on the metal oxide supports. The dashed line represents U_{diss} under standard conditions.²⁸

Tantalum (Ta) is known as one of the most corrosion resistant metals, and at low temperatures ($<150^\circ\text{C}$), tantalum is almost immune to chemical attack.²⁹ The Pourbaix diagram of Ta indicates that the range of thermodynamic stability of Ta_2O_5 lies below that of water reduction (Figure 7).³⁰ Ta_2O_5 is the thermodynamically stable phase under acidic pHs ($\text{pH}\sim 1$) and potentials (0.4 – 1.4 V) typically required for ORR. The high corrosion resistance and inertness of Ta has been attributed to a thin protective oxide film.³⁰⁻³¹

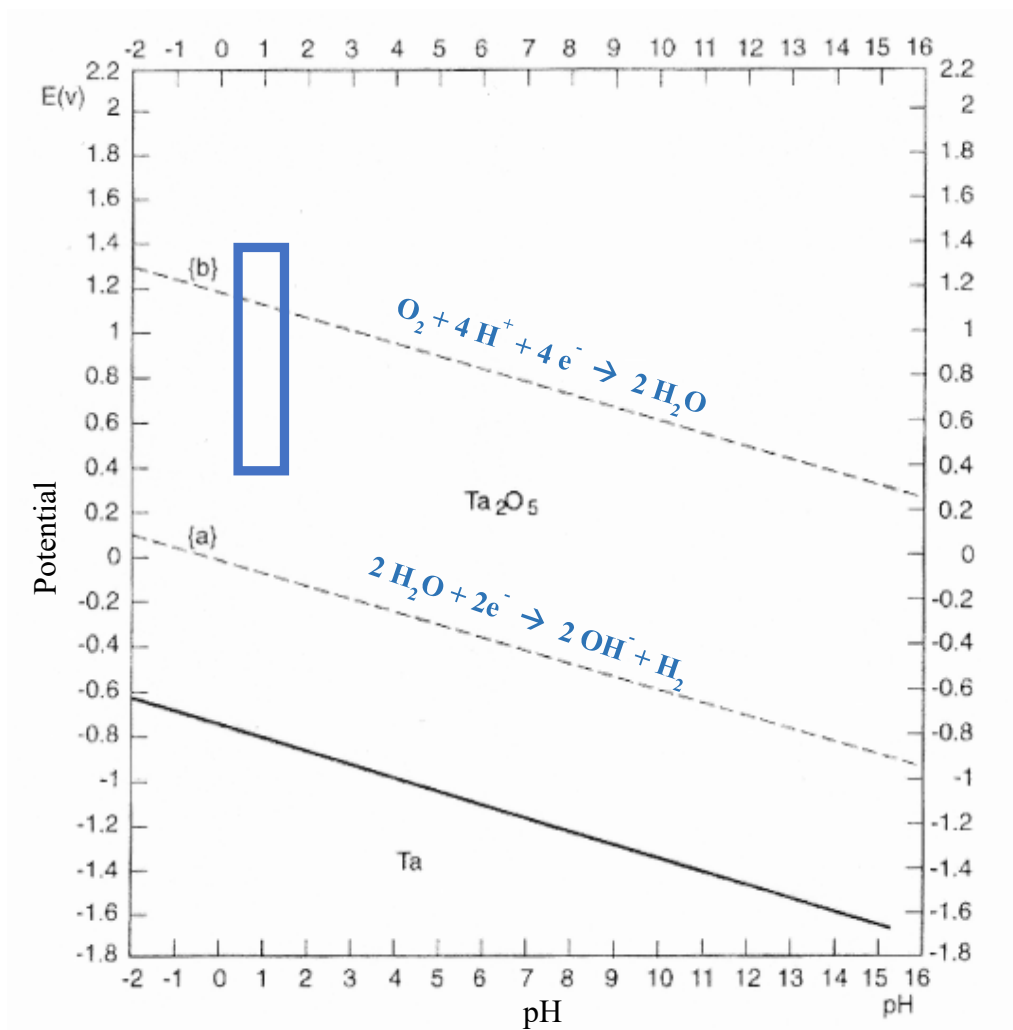


Figure 7. Pourbaix Diagram of Tantalum and Ta_2O_5 .³⁰ The blue rectangle encloses the pH and potentials typically required for the oxygen reduction reaction in PEMFC.

Tantalum is a good candidate for further investigation as a support material and prior studies have demonstrated its stability under PEMFC operation conditions.^{20, 22, 24, 32-33} The durability and corrosion resistance of different carbon-supported Pt electrocatalysts were evaluated against electrocatalysts that incorporated TaO_x with the support material. Durability was measured by calculating the change in electrochemical surface area (ECSA) under cathode conditions (Table 1).

Table 1. Change in electrochemical surface area (ECSA) for noble metal supported on carbon vs. noble metal supported on supports containing TaO_x.

Carbon-based support	ECSA decrease (m ² g ⁻¹)	Support containing TaO _x	ECSA decrease (m ² g ⁻¹)	Experimental details	Reference
Pt/C	44.5	Pt/Ti _{0.7} Ta _{0.3} O ₂	34.0	10,000 accelerated load cycling.	24
Pd/C	24.5	Pd/Ti _{0.7} Ta _{0.3} O ₂	6.2	50 cycles, 5 mVs ⁻¹ , 160 rpm.	34
Pt/Carbon Nano Tubes	38.1	Pt/Ta ₂ O ₅ /CNT	21.6	10,000 potential cycling durability tests.	22
Pt/Glassy Carbon	92.4	Pt/TaO _x /GC	68.3	5 mVs ⁻¹ , 1600 rpm.	33
Pt/Carbon	31.0	Pt/Ta ₂ O ₅ /C	17.2	10,000 cycles of accelerated durability test.	35

Even though a higher retention of the electrochemical active surface has been observed for support materials that incorporated TaO_x, prior efforts have largely focused on carbon-Ta₂O₅ support catalysts which can still result in the degradation of the support due to carbon corrosion. Other strategies have developed carbon-free supports,^{24, 34, 36} but the incorporation of TaO_x has primarily been in small quantities serving simply as a dopant rather than the main component of the support material. Both approaches limit the understanding of TaO_x as a support material and its potential to improve the durability of the electrocatalyst support.

1.4 Sol-gel Synthesis Method (High Surface Area and Porous Materials)

As discussed previously, high surface area and porosity are characteristics that a support material should have. Sol-gel synthesis is an approach that has shown success in the development of metal oxides materials with high surface area and porosity. The sol-gel synthesis route allows for metal oxide particles in the solution to agglomerate and link

together in order to form an interconnected network under controlled conditions.³⁷ The sol-gel synthesis process involves sol formation, gelation, and a drying step (Figure 8).

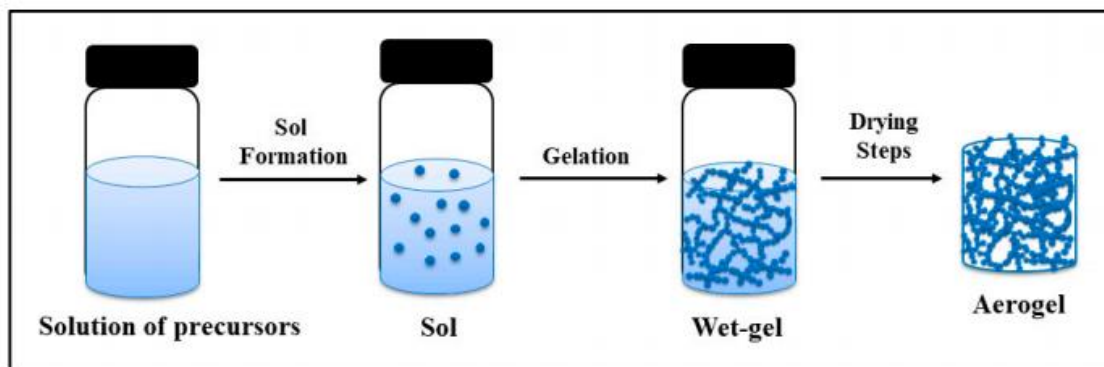
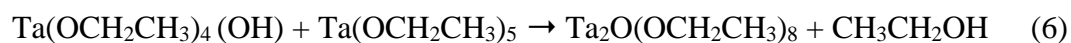
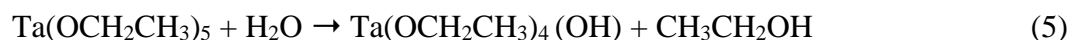


Figure 8. Schematic representation of the sol-gel method.³⁸

The sol-gel synthesis route, involving metal alkoxides $M(OR)_n$ where M can be Al, Si, Ti, V, Mo, W, or Ta, is considered a two-step polymerization reaction. The first reaction is the hydrolysis reaction that starts by the hydrolysis of an alkoxy ligand to produce a hydroxylated metal center and an alcohol (Equation 5). The second step is the condensation reaction, which occurs as the hydroxylated species condense to form oxypolymers to create oxygen bridges and the removal of water (Equation 6). In the overall reaction, the alkoxy ligand and water precursors result in a metal oxide and an alcohol (Equation 7).³⁹



There are three different drying techniques typically used to remove the liquid from the wet gel (Figure 9).⁴⁰ The first drying technique is via ambient air-drying, which leads to the formation of a dense xerogel. The second is a freeze-drying technique which

involves lowering the temperature of the solvent below its crystallization temperature and removing it as a vapor forming a cryogel. The third drying technique is a supercritical drying process which replaces the liquid phase in the wet gel with the use of a supercritical fluid, typically CO₂. By removal of the solvent under supercritical conditions, no liquid-vapor interface exists, capillary stress is prevented, and collapse of the porous structure is avoided resulting in an aerogel with high porosity, low density, and high surface area.^{38, 40}

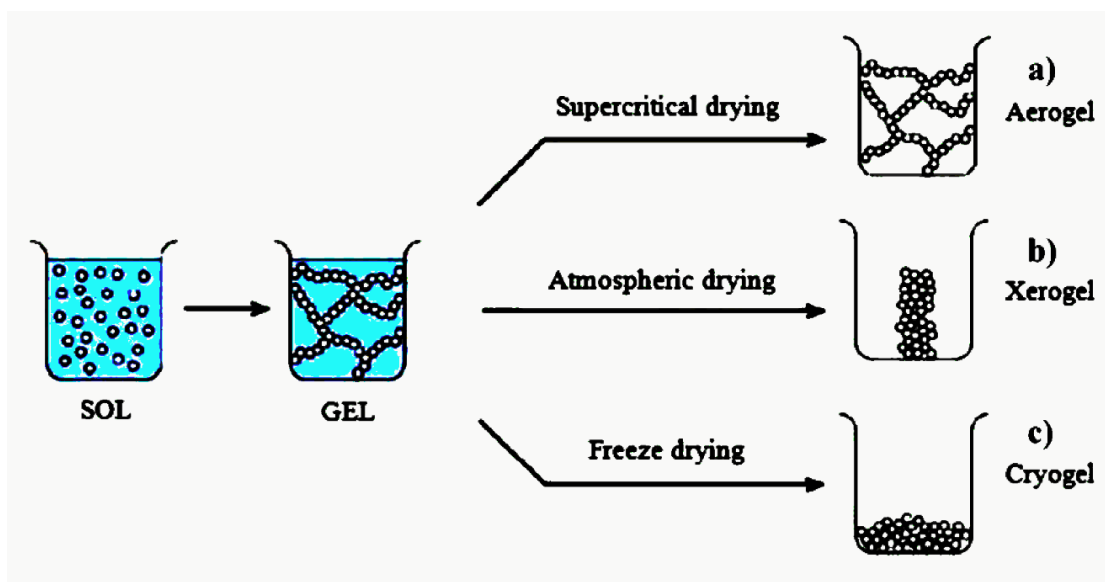


Figure 9. Three different drying techniques of a wet gel.⁴⁰

Aerogels are promising materials for the development of metal oxide supports for ORR due to several unique properties: (i) high surface area, (ii) stabilization of nanoscale particles, (iii) low controllable density, and (iv) open porosity. Different metal oxide aerogels have already been synthesized and analyzed as support materials with high surface area and porosity to replace carbon-based supports. Table 2 summarizes the results obtained from different studies on metal oxide aerogels.

Table 2. Metal oxide aerogels (surface area and pore size).

Metal Oxide Aerogel	Surface Area (m ² g ⁻¹)	Pore size (nm)	Reference
TiO ₂ aerogels	50-550	15-30	15
SnO ₂ aerogels	40-90	15-45	41
TiO ₂ aerogels	272	3-5	34
SnO ₂ aerogels	74 to 77	20-40	42
Nb ₂ O ₅ aerogels	190	2-10	43
ZrO ₂ aerogels	143-205	17-65	44
Ta ₂ O ₅ aerogels	221	2-50	45
Ta ₂ O ₅ aerogels	917	4-12	46

Although sol-gel synthesis has been recognized as a potential synthesis route to develop metal oxides supports with high surface areas and an open-pore morphology, many aerogels end up with a low surface area after undergoing thermal treatments in order to reach crystallinity and obtain sufficient electronic conductivity.^{15, 24} Hence, further research is needed in the development of aerogels that combine higher surface, high porosity, and sufficient electronic conductivity in order to successfully replace carbon-based supports.

1.5 Magnesium Reduction (Enhanced Electronic Conductivity)

Among the various metal oxides, SnO₂, TiO₂, NbO₂, and TaO₂ have shown chemical stability suitable for strong acidic conditions for PEMFC.^{22, 25-26, 32-33, 47-50} However, the choice of metal oxide used as a support material is limited when the need for high electrical conductivity is also considered. Most of these oxides are insulators (TiO₂) or wide-band gap semiconductors (SnO₂, NbO₂, and TaO₂).²⁸ For example, Ta₂O₅ has a band gap of 3.9 eV⁵¹⁻⁵² and an electronic conductivity of 3.01x10⁻¹² S/cm⁵³ while

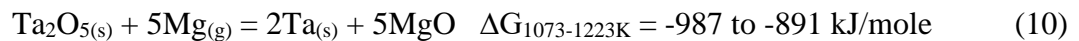
the typical electronic conductivity of carbon supports lies between 1-10 S/cm.⁹ Hence, the electronic conductivity of metal oxides must be improved before they can be considered as potential alternative materials to carbon-based supports for PEMFC application.

Although there are several ways to increase the electronic conductivity of a metal oxide,^{15, 24, 54-57} increasing their conductivity through reduction by using magnesium (Mg) as a reducing agent is a favorable approach for the following reasons: (i) the metal produces a promising way for the preparation of nano-sized metal oxide powders; (ii) the reduction temperature is low and adjustable; (iii) handling of Mg powder is relatively easy; (iv) the by-product (MgO) can be easily eliminated by acid leaching; and (v) the morphology of the initial material can be preserved.⁵⁸⁻⁶¹

Furthermore, Mg reduction of some metal oxides is thermodynamically favorable because the active metal (Mg) has a higher oxygen affinity than the metal oxide. Based on the Ellingham diagram (Figure 10), the reduction of tantalum using Mg is thermodynamically favorable because the line representing the reaction of magnesium (Equation 8) lies below the line representing the reaction of tantalum (Equation 9).



Since the reaction line of magnesium lies below that of tantalum's, ΔG is negative, and the reaction is thermodynamically favorable.⁶² The overall reaction is shown in Equation 10, which shows that the driving force for the reaction of tantalum is tremendous.⁶⁰



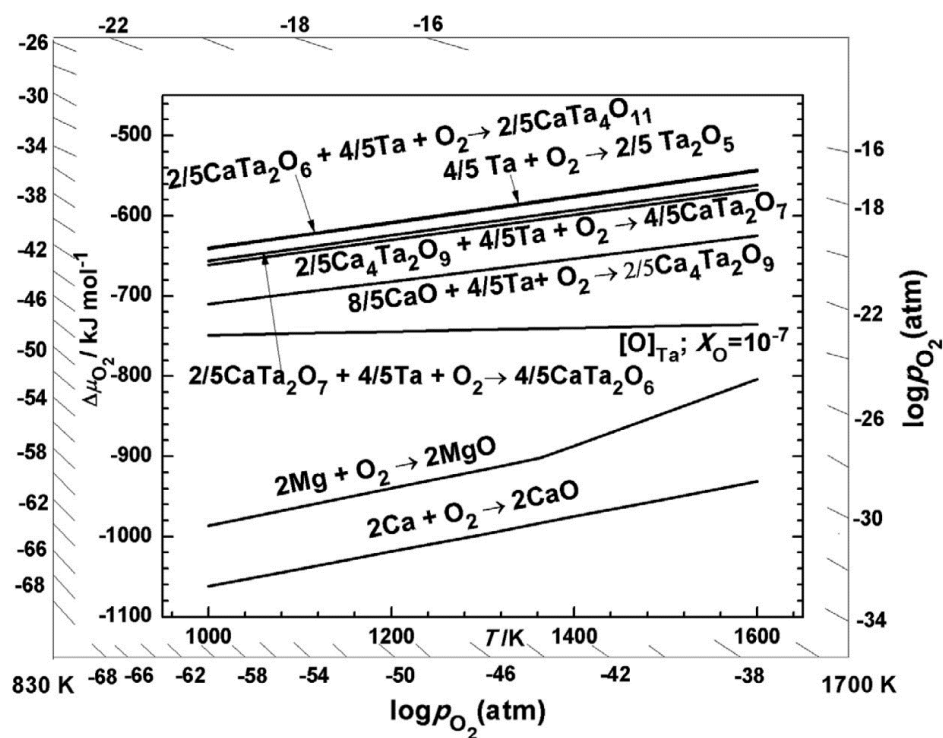


Figure 10. Ellingham diagram.⁶³

Overall, Mg reduction will lead to structural transformation and intrinsic band gap changes of the metal oxide that may enhance the electronic conductivity of the material. Prior work using Mg as a reducing agent under a reducing atmosphere (H_2/Ar) resulted in a highly conductive black ZrO_{2-x} by decreasing its broad band gap of 5-7 eV to 2.1 eV, changing its oxidation number from Zr^{+4} to Zr^{+3} , and forming oxygen vacancies.⁵⁴ Another study modified the intrinsic band gap of TiO_2 via Mg reduction which resulted in a higher conversion efficiency of solar light energy to water evaporation.⁶⁴ Lastly, a prior study on the electrical conductivity in oxygen-deficient phases of Ta_2O_5 observed a trend of increasing electronic conductivity with decreasing oxygen content.⁶⁵ The electronic conductivity increased in the following way $\text{Ta}_2\text{O}_5 < \text{Ta}_2\text{O}_2 < \text{Ta}_2\text{O}$. Experimentally, the reduction of tantalum oxide by using Mg as a reducing agent has been carried it out

successfully.⁵⁸⁻⁶⁰ However, prior studies have largely focused in the reduction of TaO_x to tantalum metal with the goal of simply producing a pure metal instead of increasing its electronic conductivity. Additionally, the effect of Mg reduction on TaO_x aerogels has not been studied.

1.6 Project Motivation and Objectives

Tantalum oxide (TaO_x) is resistant to corrosion under the oxidative potentials encountered in the oxygen reduction reaction for proton exchange membrane fuel cells. Although prior studies have used tantalum in electrocatalyst supports, most of the prior work have largely focused on carbon-Ta₂O₅ supports, which can still result in the degradation of the support, or they have limited the use of tantalum to a dopant rather than the main component in the support.^{22, 32-33}

The motivation of this project was to develop TaO_x aerogels that could serve as potential carbon-free support materials for the ORR in PEMFCs. To our knowledge, no prior study has explored the effect of thermal treatments and reduction of TaO_x aerogels to modify their crystal structure and improve their electronic conductivity. The hypothesis tentatively assumed that the reduction of TaO_x aerogels using Mg as a reducing agent will increase the electronic conductivity of TaO_x aerogels while retaining the properties of large surface area and porous morphology.

The specific research objectives were the following: i) synthesize high surface area and porous TaO_x aerogels via sol-gel synthesis and supercritical drying to determine the effect of thermal treatments in air in order to obtain two different precursors (amorphous vs crystalline); ii) determine the effect of thermal reduction (using Mg as a

reducing agent) on the morphology, crystallinity, and degree of reduction of TaO_x aerogels; and iii) analyze the effect of reduction on the electronic conductivity of TaO_x aerogels. The results of this project aimed to contribute to the scientific knowledge concerning the design and development of a highly stable carbon-free support catalyst for the oxygen reduction reaction in proton-exchange membrane fuel cells.

2. MATERIALS AND METHODS

2.1 Chemicals

Tantalum ethoxide ($\text{Ta}(\text{OC}_2\text{H}_5)_5$), 200 proof anhydrous ethyl alcohol ($\text{C}_2\text{H}_6\text{O}$), nitric acid (HNO_3), and Mg powder >99.9% (40-45 μm in size) were obtained from Sigma Aldrich. Washed acetone was obtained from the Chemistry department at Texas State University. All reagents were used without further purification.

2.2 Synthesis of Tantalum Oxide Gels

Tantalum oxide aerogels and xerogels were synthesized using a sol-gel synthesis method adapted from a previously reported procedure.⁴⁶ Two solutions (A & B) were prepared in the following way. Solution A, prepared inside an argon-filled ($\text{H}_2\text{O} \leq 1.0$ ppm) glove box, consisted of 1.5 g (3.7 mmol) of tantalum ethoxide dissolved in 7.9 g (171 mmol) of ethyl alcohol. Solution A was magnetically stirred (600 rpm) for 10 minutes. Solution B, prepared outside the glovebox, consisted of 198.6 μL of ultrapure water (>18 M Ω) using PureLab Classic DI instrument, 626 μL of ethanol, and 37.6 μL nitric acid. Solution B was magnetically stirred (400 rpm) for 10 minutes. Subsequently, solution A was added into solution B. The final solution was stirred for 10 minutes and then transferred to a plastic vial where it remained still. The solution gelled after a certain time (~ 2–3 h) and the wet gel was aged for an additional 72 hours at room temperature. The gel was washed with ethanol once a day for three days. The gel was then dried either via ambient air-drying for 24 h at 60 °C to form a xerogel or under supercritical conditions (73.8 bars, 31 °C) where the ethanol was exchanged for CO_2 and then removed using a Leica EM CPD 300 instrument to form an aerogel.

2.3 Thermal Treatments

Tantalum oxide aerogels were thermally treated in a muffle furnace (Thermolyne, Thermo Scientific, Inc.) at 550 °C or 850 °C in air for 2 hours using a ramp rate of 10 °C/min.

2.4 Magnesium Reduction Method

The thermal treatment using metallic magnesium as a reducing agent was performed by modifying previously reported procedures.^{54, 64} Approximately, 0.30 g of TaO_x aerogel was mixed and ground with approximately 0.30 g of Mg powder (50:50 wt%) using an agate mortar and pestle. The sample was transferred to a quartz vial and sealed under vacuum with an in-house vacuum system. Mg reduction method was performed by heating the sealed vial up to 600 °C for 4 h under an argon atmosphere with a ramp rate of 10°C/min in a tube furnace (Lindberg Blue M, Thermo Scientific). After the Mg reduction method, the quartz vial was cooled down to room temperature and taken out of the tube furnace. Subsequently, the quartz vial was transferred to an argon-filled (H₂O ≤ 1.0 ppm) glove box, opened, and transferred to a clean vial to prevent the reduced material from reacting with atmospheric oxygen. The clean vial with the reduced sample remained in the glovebox overnight before it was taken out to ambient atmosphere.

2.5 Chemical Leaching

To remove MgO impurities, the reduced samples were chemically leached in 100 mL of 0.3 M HCl solution under magnetic stirring for 1 h. The sample was subsequently

rinsed five times in ultrapure water, two times in acetone, and then recovered by centrifugation (1690 RFC, 3,000 rpm, 3 min, thermo, Sorvall ST16). Lastly, the sample was dried overnight at 60°C in air.

2.6 Sample Notations

The notations used for the different TaO_x aerogel samples are listed in Table 3 and described as follows: the as-prepared TaO_x aerogel's notation is (Ta-Ap), for the 550 °C thermally treated TaO_x aerogel (Ta-550), for the 850 °C thermally treated TaO_x aerogel (Ta-850), for the as-prepared TaO_x aerogel after Mg reduction (Ta-Ap-Mg), for the 850-thermally treated aerogel after Mg reduction (Ta-850-Mg), for the as-prepared TaO_x aerogel after Mg reduction and chemical leaching (Ta-Ap-Mg-CL), and for the 850-thermally treated aerogel after Mg reduction and chemical leaching (Ta-850-Mg-CL).

Table 3. Notation used to label different TaO_x aerogels.

Material	Thermal treatment	Mg reduction method	Chemical Leaching	Label
TaO _x aerogel	No-treatment	No	No	Ta-Ap
TaO _x aerogel	550 °C	No	No	Ta-550
TaO _x aerogel	850 °C	No	No	Ta-850
TaO _x aerogel	No-treatment	Yes	Yes	Ta-Ap-Mg-CL
TaO _x aerogel	850 °C	Yes	Yes	Ta-850-Mg-CL

2.7 Physical and Structural Characterization

Powder X-ray diffraction (XRD) measurements were conducted using a Bruker AXS D8 Advance powder X-ray diffractometer with a Cu K α ($\lambda = 1.5406 \text{ \AA}$) radiation source, operating at 40 kV and 25 mA and a high-resolution energy-dispersive 1D Linxeye XE detector. The scan range of 2θ was $15^\circ < 2\theta < 85^\circ$ with a 0.01° increment. The powder diffractograms of metallic Ta (PDF 01-088-2338), MgO (PDF 96-900-6750),

Ta₂O₅ (00-019-1298), TaO (PDF 03-065-6750), and Ta₂O (PDF 01-074-2305) were obtained from the crystallography open database (COD) were used as references.

Nitrogen physisorption measurements were obtained using a Micromeritics ASAP 2020 surface area and porosimetry analyzer. Before analysis, the samples were degassed under vacuum at 120 °C for 16 h. Brunauer–Emmett–Teller (BET) surface areas were obtained from the nitrogen physisorption isotherms. Mean pore diameters and cumulative pore volumes were calculated from the desorption isotherm using the Barrett–Joyner–Halenda method (Micromeritics Microactive software, version 4.02).

Scanning electron microscopy (SEM) images and energy dispersive X-ray spectroscopy (EDS) measurements of the materials were obtained using a Helios NanoLab 400 Dual Beam Field Emission Scanning Electron Microscopy. For sample preparation, powders were dispersed in isopropanol, sonicated for 5 minutes, deposited on an aluminum sample holder, and further dried in an oven at 60 °C for 5 minutes. Thermogravimetric analysis (TGA) was used to analyze the different weight loss processes occurring when increasing temperature. TGA measurements (TA Instruments Q50) were performed at a constant heating rate of 10 °C/min in air from 25 °C to 800 °C.

2.8 Electronic Measurements

The electronic conductivities of the materials were determined with a conductivity cell made in-house of two stainless steel electrodes (area = 1.27 cm²) and an insulating ring. Approximately 100 mg of material was introduced between the two electrodes (Figure 11). The electrodes were pressed using a pressure of 20 psi transferred to the conductivity cell and measured at room temperature.

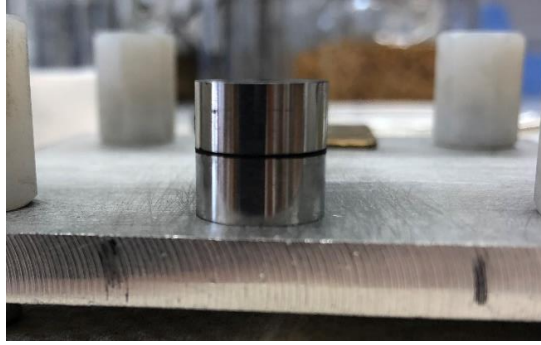


Figure 11. Stainless steel electrodes (gray) with the material introduced in between the two electrodes (black).

Two-point probe measurements were obtained using a constant voltage (± 0.1 V) applied to the conductivity cell made in-house (Figure 12) using an Arbin Instruments BT-2043 potentiostat/galvanostat. The current was monitored until quasi-steady state was reached (~ 5 min) and the resistance was determined using Ohm's law, $R = V/I$. The thickness and diameter of the pellet were measured using a micrometer (Mitutoyo, USA). The electrical conductivity, σ_{elec} (S cm^{-1}), was calculated from the experimentally measured values using the equation $\sigma = l/(R \cdot A)$, where l is the thickness of the sample, R is the measured resistance in Ω , and A is the cross sectional area.

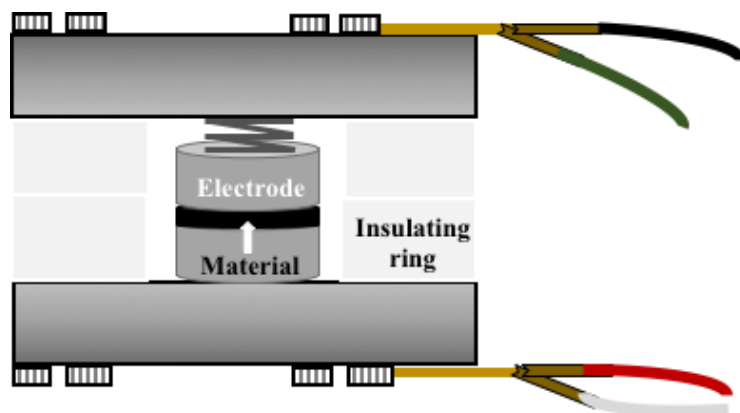


Figure 12. Schematic diagram of the conductivity cell made in-house of two stainless steel electrodes, insulating rings, and the pressed material in between the electrodes to obtain two-point probe measurements.

3. RESULTS AND DISCUSSION

3.1 Effect of Thermal Treatment in the Crystal Structure of TaO_x Aerogels

To study the effect of thermal treatment on as-prepared TaO_x gels, thermogravimetric analysis (TGA) was performed from 25 °C to 800 °C with a heating rate of 10 °C /minute in air atmosphere. Figure 13 represents the results obtained from the TGA analysis of an as prepared TaO_x xerogel.

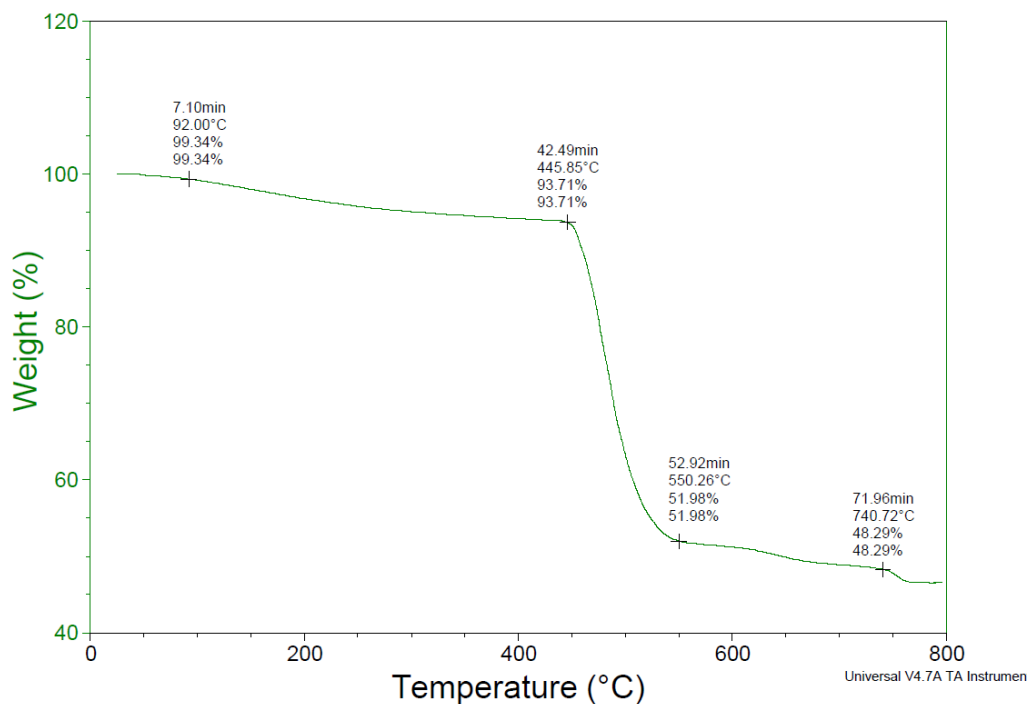


Figure 13. Thermogravimetric Analysis (TGA) curve of TaO_x xerogel.

Technical issues with the thermogravimetric equipment limited further analysis using the aerogel samples; however, the data obtained from TaO_x xerogel were taken as representative of the effects of heating in air for the TaO_x aerogels. The weight loss at temperatures lower than 400 °C was attributed to the dehydration and decomposition of organic compounds from organic precursors used in the synthesis of TaO_x aerogels. The significant 45% weight loss observed at temperatures higher than 450 °C was attributed

to the removal of oxygen or hydroxyl groups, but further analysis needs to confirm this. TGA does not alone prove a phase transition but additional observations of an exothermic peak centered at 386.7 °C in a differential thermal analysis supported this assessment.⁵¹

Based on the results obtained in the TGA analysis, thermal treatments were performed on TaO_x aerogels at different temperatures (550 °C and 850 °C) for 2 hours in air in a muffle furnace. The changes in the structure during heating were determined by X-ray diffraction (XRD) analysis. Figure 14 summarizes the results obtained from the XRD analysis of TaO_x aerogels.

As-prepared TaO_x aerogels (Ta-Ap) have an amorphous structure as no defined peaks are observed within the XRD pattern, but only broad features indicating a weak organization of the atoms. However, as the temperature increased to 550 °C, a mild crystal reorganization took place and broad peak were observed. Subsequently, the thermal treatment at 850 °C resulted in an important structural reorganization since a phase transition from an amorphous structure to a monoclinic Ta₂O₅ crystal structure according to standard reference for Ta₂O₅ (00-019-1298) was observed on the XRD pattern. A prior study indicated that the high crystallinity of materials can improve the electrical conductivity in comparison to amorphous ones.¹⁵ Furthermore, it has been observed that Ta₂O₅ amorphous materials have a higher band gap and a lower electronic conductivity compared to Ta₂O₅ crystalline materials.⁶⁵⁻⁶⁶ Generally in electrocatalysis, a combination of surface reactivity, electronic conductivity, ionic conductivity, separation of electron-hole pairs, and facile mass transport of molecules must be provided in order to enhance the molecular conversion and obtain high performance.¹⁴

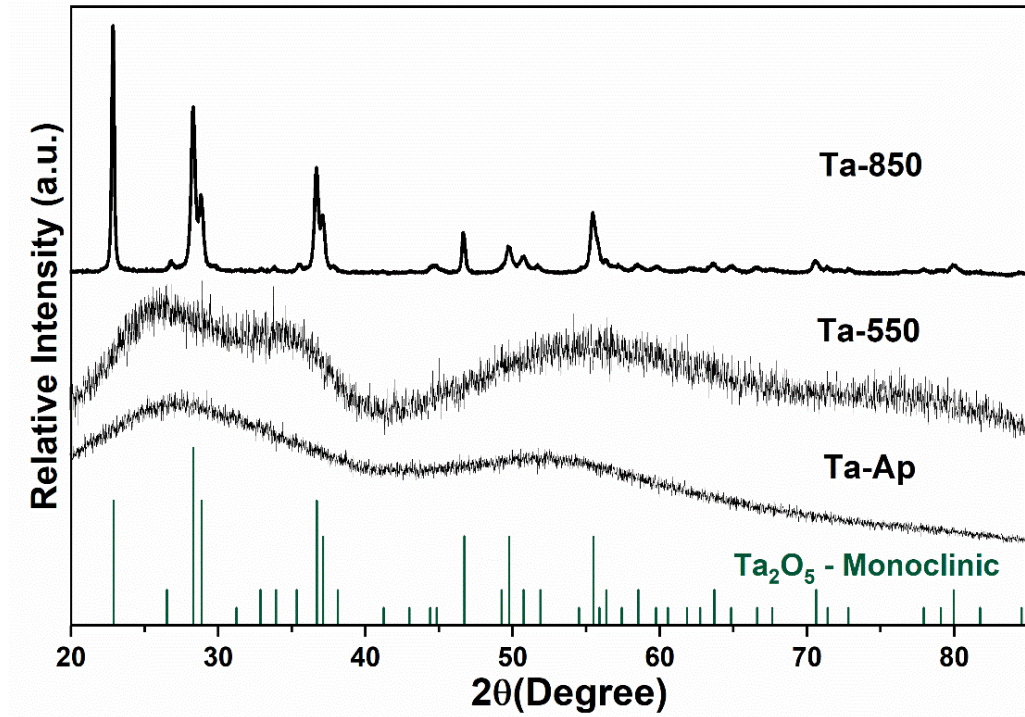


Figure 14. X-ray diffraction (XRD) of TaO_x aerogels obtained at different temperatures (as-prepared, 550°C, and 850°C); diffraction peaks corresponding to monoclinic Ta₂O₅ reference (00-019-1298) are shown at the bottom of the figure.

3.2 Effect of Mg Reduction in TaO_x Aerogels Physical Properties

Since Ta₂O₅ is an electronic insulator with a wide band gap of 3.9 eV and an electronic conductivity of 3.01×10^{-12} S/cm, its electronic conductivity must be modified before Ta₂O₅ can be considered as an alternative material to replace carbon-based supports in fuel cells.^{9, 52-53} Hence, thermal treatments to the TaO_x aerogels with metallic magnesium were carried out. The overall reaction would promote oxygen-deficient phases of TaO_x aerogels by promoting tantalum reduction (Equation 11).^{54, 58-60}



The overall Mg reduction process was performed to as-prepared TaO_x aerogels (Ta-Ap) and TaO_x aerogels heated to 850°C in air (Ta-850) as described in the

experimental methods section. Figure 15 (g) shows a schematic illustration of the Mg reduction steps performed to the TaO_x aerogels.

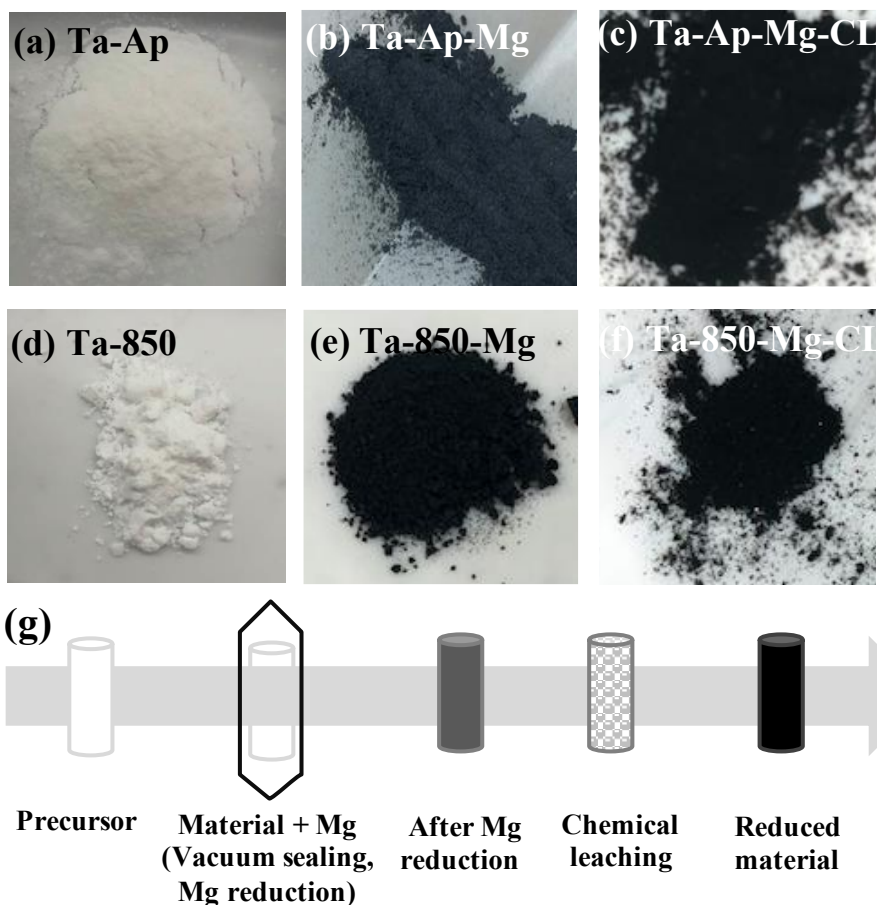
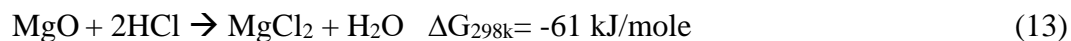


Figure 15. (a-c) Pictures of the Mg reduction steps performed to the as-prepared TaO_x aerogel; (d-f) pictures of the Mg reduction steps performed to the 850-thermally treated TaO_x aerogel; (g) schematic illustration of the Mg reduction steps.

Figures 15(a) and (d) present visually observed physical properties between Ta-Ap and Ta-850 precursors prior to their reduction using Mg as a reducing agent. Overall, the heat treatment at 850°C in air did not promote any visible color change to Ta-850 sample since its color remained white as Ta-Ap. The only visible changes observed between Ta-Ap and Ta-850 were the textures of the grains and the apparent volumes. The grains of Ta-Ap sample were fluffy and voluminous while the grains in the Ta-850

sample were dense and compacted. These visibly observed changes were consistent with the weight loss of TaO_x aerogel at temperatures higher than 450 °C according to TGA analysis and the increase in crystallinity observed in the XRD analysis. After Mg reduction, a dramatic color change is observed visually between Ta-Ap-Mg and Ta-850-Mg samples. Ta-Ap-Mg turned gray in color while Ta-850-Mg turned black. The gray color observed in Ta-Ap-Mg is attributed to the presence of unreacted Mg powder because after the chemical leaching step, the gray color turned black. Removal of the gray color is an indication that any unreacted Mg and MgO impurities were successfully removed by the chemical leaching step according to Equations 12 and 13.⁵⁸⁻⁶⁰



Although the color change is a physical property, a prior study indicated that a color change implies the modification of the material's optical properties as a result of a reduced bandgap by the creation of oxygen vacancies within the lattice.⁵⁴ A black color in a material indicates the ability of the material to absorb light in the whole visible light range. Furthermore, a lower band gap in TaO_x materials is associated with a higher electronic conductivity.⁶⁵

3.3 Effect of Mg Reduction on The Morphology of TaO_x Aerogels

High surface area is an important feature that a support material needs to have for a better distribution of the catalyst, an improved utilization of the catalyst, and a higher reduction of particle agglomeration.¹²⁻¹⁶ In a similar manner, adequate pore structure (i.e. mesoporous morphology) allows for a better mass transport of gases onto the catalyst

surface and a better removal of the reaction products from the catalyst layer in the fuel cell.¹⁵

The morphologies of the TaO_x aerogels were evaluated before, during, and after the Mg reduction process using scanning electron microscopy (SEM). The Ta-Ap sample showed a nanoparticle morphology composed of spherical particles that are highly compacted and dense (Figure 16a). The particle diameter was heterogeneous approximately 10 to 300 nm. In contrast, the Ta-850 sample exhibited a more homogeneous network of interconnected spherical nanoparticles with diameters in the range of 20 to 90 nm (Figure 16d). The difference in morphology observed in Ta-850 was attributed to the coalescence of particles due to the 850 °C thermal treatment performed prior to the Mg reduction method.

After the Mg reduction method, the spherical morphology of the particles observed in Ta-Ap-Mg was retained, but there was a decrease in the particle diameter to <100 nm (Figure 16b). On the other hand, the average particle diameter of Ta-850-Mg sample increased between 100 to 200 nm (Figure 16e).

Subsequently, after the chemical leaching step (Figure 16c and 16f) the main difference observed between the morphologies of Ta-Ap-Mg-CL and Ta-850-Mg-CL was the size of the particles. Ta-Ap-Mg-CL had a heterogeneous morphology formed of smooth large particles and rough small particles while the Ta-850-Mg-CL had a homogeneous morphology composed of particles roughly even in size.

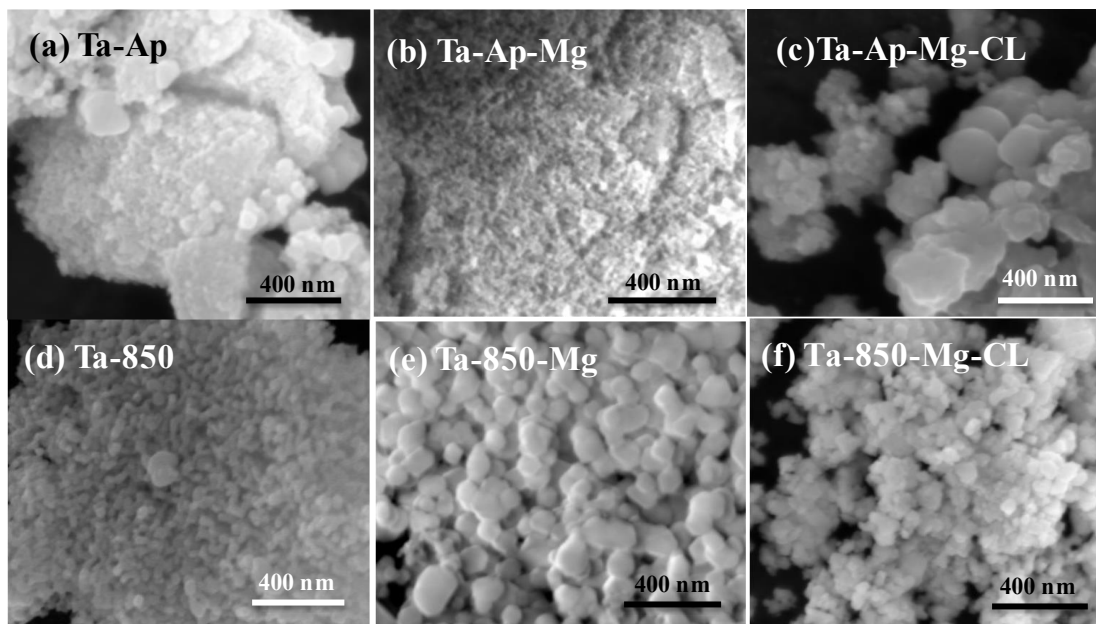


Figure 16. (a-c) Scanning Electron Microscopy (SEM) pictures of the Mg reduction steps performed to the as-prepared TaO_x aerogel; (d-f) pictures of the Mg reduction steps performed to the 850-thermally treated TaO_x aerogel.

3.4 Effect of Mg Reduction on The Chemical Composition of TaO_x Aerogels

Changes of the chemical composition was determined by Energy Dispersive X-ray Spectroscopy (EDS). The elemental composition in TaO_x aerogels was dramatically affected by the temperature, Mg reduction, and chemical leaching treatments (Figure 17). EDS elemental analysis showed that Ta was present and evenly distributed throughout the structure of the aerogels before and after the Mg reduction process. Prior to Mg reduction, the 850°C-thermal treatment performed to the TaO_x aerogel resulted in an important reduction of carbon and oxygen content in comparison to the TaO_x aerogel that did not undergo thermal treatment. The removal of organic residues such as ethanol or carbon by thermal treatment at 850°C in air is also consistent with the results observed from TGA analysis.

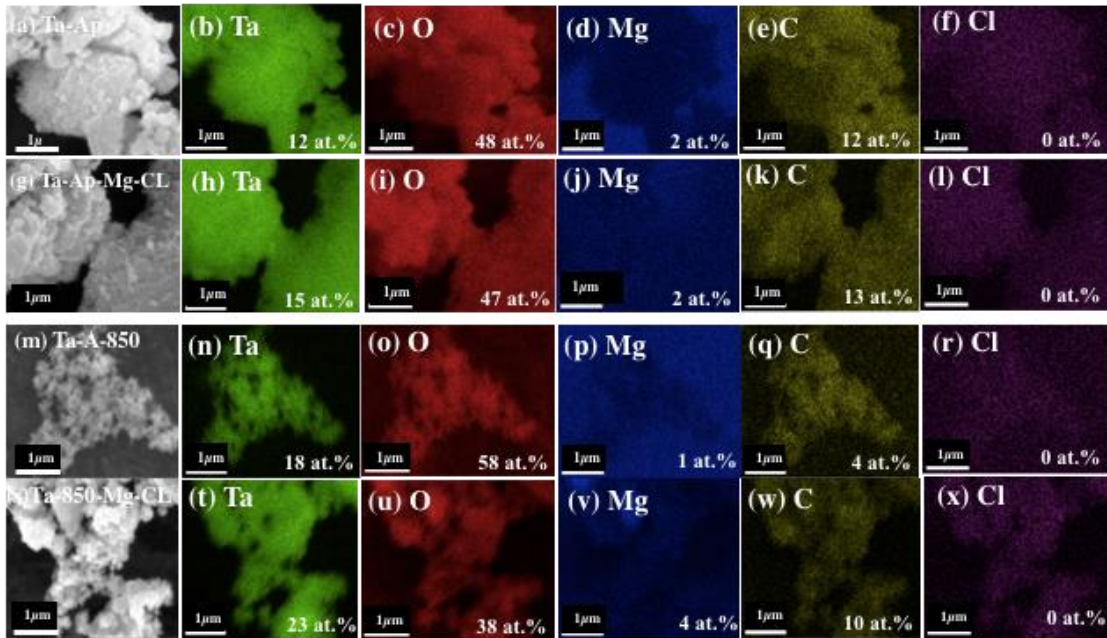


Figure 17. Scanning electron microscopy (SEM) images of (a) Ta-Ap, (g) Ta-Ap-Mg-CL, (m) Ta-A-850, and (s) Ta-850-Mg-CL; element map composition of tantalum (b, h, n, t), oxygen (c, i, o, and u), magnesium (d, j, p, and v), carbon (e, k, q, and w), and chlorine (f, l, r, and x).

Table 4 summarizes the relative elemental composition based on EDS analysis, normalizing to an atomic ratio of one for Ta. The most important observations were the change of oxygen and carbon content within the structure. For example, the reduction of TaO_x aerogel precursors with Mg metal resulted in a decrease of the tantalum to oxygen atomic ratio in both Ta-Ap and Ta-850. After reduction, Ta-Ap-Mg-CL, which started with an amorphous structure, showed a relative oxygen reduction of 0.8 while Ta-850-Mg-CL, which started with a crystalline structure, showed a higher oxygen reduction of 1.7. Such high difference suggests that the starting crystallinity of the precursor may play an important role in the reduction mechanism with magnesium. A greater removal of oxygen content is achieved when the precursor has high crystallinity.

Furthermore, the high atomic ratio of carbon observed in Ta-Ap is attributed to residual carbon from the ethanol used during the synthesis of TaO_x aerogels. Because the amount of carbon is significantly high in the reduced Ta-Ap-Mg-CL sample, further analysis is recommended. Although carbon can increase the electronic conductivity of the material, it can also lead to degradation of the material due to corrosion.

Lastly, the presence of Mg was related to small impurities remaining after acid leaching and the contribution from the sample holder use during analysis. Although the presence of Cl was also observed, its relative atomic ratio was virtually zero.

Table 4. Atomic ratio determined from Energy Dispersive X-ray Spectroscopy (EDS) analysis of TaO_x aerogels.

Material	Ratio Ta : O : Mg : C : Cl	Stoichiometry	Oxygen difference
Ta-Ap	1.0 : 3.9 : 0.2 : 1.0 : 0.0	TaO _{3.9}	0.8
Ta-Ap-Mg-CL	1.0 : 3.1 : 0.1 : 0.9 : 0.0	TaO _{3.1}	
Ta-850	1.0 : 3.3 : 0.1 : 0.2 : 0.0	TaO _{3.3}	1.7
Ta-850-Mg-CL	1.0 : 1.6 : 0.2 : 0.4 : 0.0	TaO _{1.6}	

3.5 Effect of Mg Reduction in The Crystal Structure of TaO_x Aerogels

The effect of reduction in the aerogels' crystal structures were analyzed by X-ray Diffraction (XRD). Figure 18 shows the XRD patterns of Ta-Ap, Ta-Ap-Mg, and Ta-Ap-Mg-CL samples. Powder diffraction references taken from the crystallography open database (COD) were used for comparison with measured samples. The green, red, gray, and blue lines at the bottom of Figure 18 represent the diffraction patterns of TaO, MgO, metallic Ta, and Ta₂O respectively.

XRD patterns showed that Ta-Ap only had broad features due to a weak organization of its atoms within the amorphous structure. However, after Mg reduction, the XRD of Ta-Ap-Mg showed four peaks (111), (200), (220) and (311) at 2θ values of

35.14°, 41.62°, 57.75°, and 70.78° corresponding to the reference pattern of TaO crystal structure according to standard reference (PDF 03-065-6750).

The XRD pattern of Ta-Ap-Mg also showed one peak at a 2θ value of 35.47°, corresponding to the (111) plane of metallic tantalum and two peaks at 2θ values of 42.80° and 62.14° respectively corresponding to the (002) and (022) planes of MgO. Although other small peaks were distinguishable along the diffractogram, these small phases were not characterized. The reduction of Ta-Ap by Mg was considered successful because of the phase transition to TaO crystal structure and the appearance of MgO peaks. It is important to mention that the changes observed in Ta-Ap should not only be attributed to the reduction by Mg, but also to the thermal treatment at 600°C performed during the reduction procedure. While the reduction of Ta-Ap by the strong Mg reducing agent leads to a decrease in its oxygen content, the thermal treatment at 600°C may affect the arrangement of its atoms and hence its crystal structure. Therefore, the 600°C thermal treatment and reduction with magnesium are both factors that contribute to the final structure of Ta-Ap-Mg-CL.

Lastly, the XRD pattern of Ta-Ap-Mg-CL did not have MgO peaks any longer suggesting that the chemical leaching step was successful in removing MgO impurities. A small peak at a 2θ value of 37.94° was also observed and attributed to Ta₂O crystal structure, but no other peaks corresponding to this crystal structure were observed.

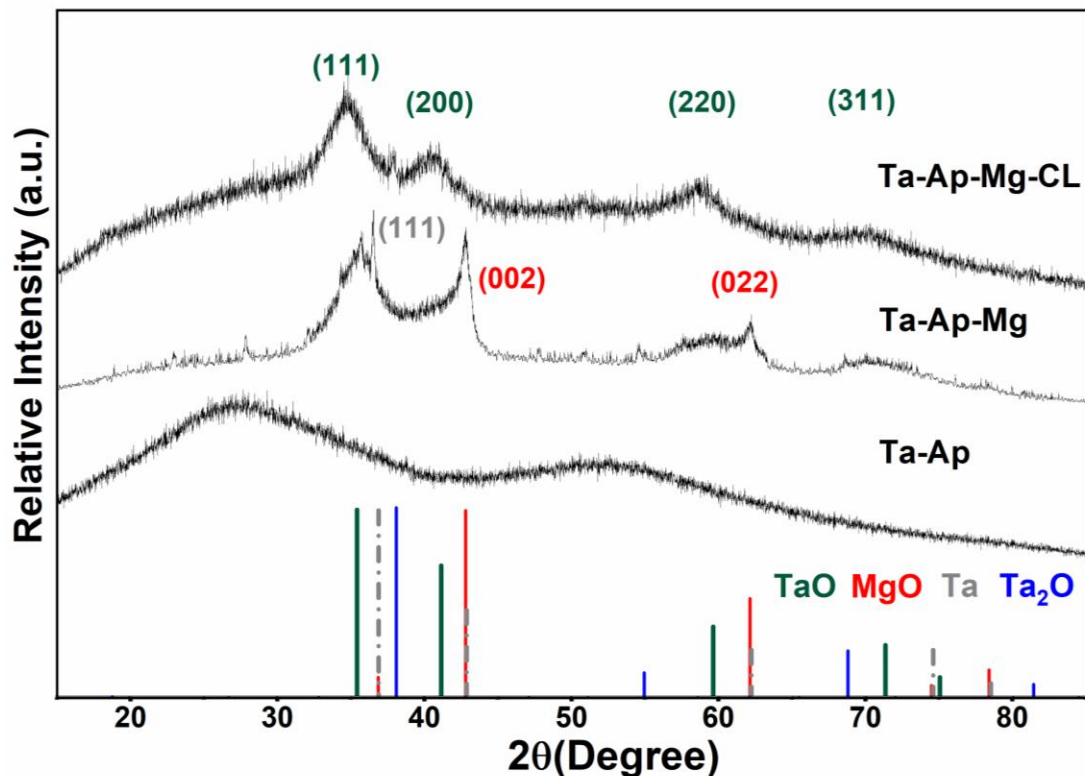


Figure 18. X-ray diffraction (XRD) patterns of as-prepared TaO_x aerogel (Ta-Ap), Ta-Ap after Mg reduction (Ta-Ap-Mg), and Ta-Ap-Mg after chemical leaching (Ta-Ap-Mg-CL); diffraction peaks corresponding to standard references for TaO, MgO, metallic Ta, and Ta₂O are shown at the bottom of the figure.

XRD analysis was also performed in the samples thermally treated to 850 °C in air, subsequently reduced using Mg metal, and then chemically leached. The XRD patterns of Ta-850, Ta-850-Mg, and Ta-850-Mg-CL are shown in Figure 19. The XRD analysis indicated that the reduction of Ta-850 using Mg as a reducing agent resulted in a phase transformation from a monoclinic Ta₂O₅ to a Ta₂O crystal structure according to standard reference Ta₂O (PDF 01-074-2305). The phase transformation was supported by the peaks corresponding to Ta₂O₅ crystal structure disappearing and the three (220), (400), and (422) peaks at 2θ values of 38.07°, 54.94°, and 68.79° corresponding to Ta₂O crystal structure appearing. The XRD analysis after Mg reduction showed one (111) peak

at a 2θ value of 35.47° corresponding to metallic Ta and two (002) and (022) peaks at 2θ values of 42.80° and 62.14° attributed to MgO. After chemical leaching, these peaks were no longer observed. Since Ta-850 had undergone a thermal treatment at 850°C prior to Mg reduction, its phase transformation is entirely attributed to the reduction by Mg metal and not to the 600°C thermal treatment performed during the reduction procedure.

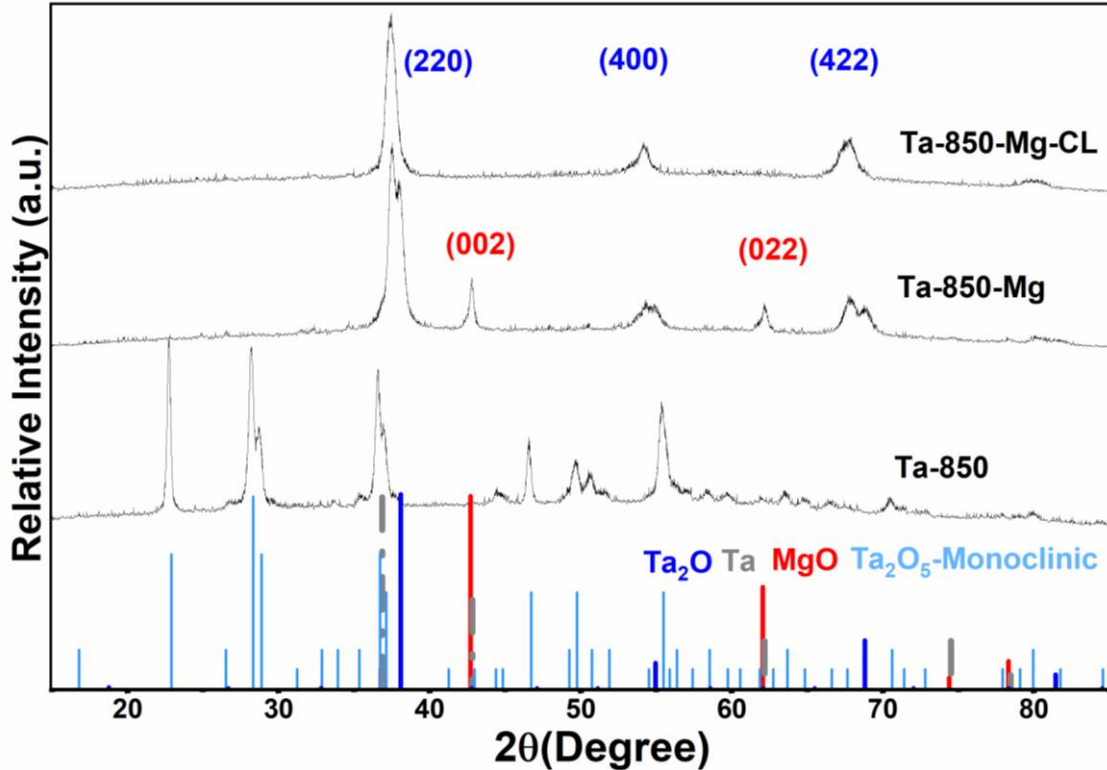


Figure 19. X-ray diffraction (XRD) patterns of 850-thermally treated TaO_x aerogel (Ta-850), Ta-850 after Mg reduction (Ta-850-Mg), and Ta-850-Mg after chemical leaching (Ta-850-Mg-CL); diffraction peaks corresponding to the dark blue, gray, red, and light blue vertical lines at the bottom represent the diffraction patterns of Ta_2O , metallic Ta, MgO, and monoclinic Ta_2O_5 respectively.

3.6 Analysis on The Degree of Reduction in TaO_x Aerogels

When both of the XRD patterns of Ta-Ap and Ta-850 were compared and a stoichiometric analysis of the degree of reduction was calculated based on XRD standard reference patterns, it was observed that the degree of reduction was different for each of

the samples (Table 5). The aerogel previously heated to 850 °C in air, Ta-850, had an initial tantalum to oxygen ratio of 1 to 2.5 based on its initial Ta₂O₅ crystal structure. However, after reduction by Mg, its Ta to O content decreased to 1 to 0.5 based on its final Ta₂O crystal structure. More than 75% of the oxygen content in Ta-850 sample was removed after reduction by Mg and chemical leaching. In comparison, based on the XRD analysis, the initial stoichiometry of Ta-Ap sample was unknown because it did not present a definite crystal structure. However, its final tantalum to oxygen ratio was 1 to 1 based on the TaO crystal structure achieved after reduction by Mg and chemical leaching.

The results indicated that the crystalline precursor (Ta-850) reached a higher degree of reduction compared to the amorphous precursor (Ta-Ap) suggesting that crystallinity plays an important role during the Mg reduction process. The role of the precursor's crystallinity observed in the XRD analysis is in agreement with the results observed in the EDS analysis. Prior studies had suggested that reduction of the surface of a metal oxide proceeds with a rate constant that depends on the orientation of the surface plane, the extent of reduction, and the nature of the surface defects.⁶⁷⁻⁶⁸ The position of oxygen atoms and number of bonds to surrounding atoms should influence their removal with a different degree of difficulty. Hence, the degree of reduction is expected to be dependent upon the initial structure of the precursor.

Table 5. Degree of reduction based on standard references of XRD patterns.

Sample	Crystal Structure	Reference	Atomic ratio	Degree of Reduction
-	-	Ta	TaO ₀	High  Low
Ta-850-Mg-CL	Ta ₂ O	Ta ₂ O	TaO _{0.5}	
Ta-Ap-Mg-CL	TaO	TaO	TaO ₁	
Ta-850	Ta ₂ O ₅	Ta ₂ O ₅	TaO _{2.5}	

3.7 Analysis of Oxygen Concentration

A subsequent study of the peak location, d-spacing, lattice constant, and crystal size of both reduced samples, Ta-Ap-Mg-CL and Ta-850-Mg-CL, was done based on the data obtained from the XRD analysis. The parameters of the reduced samples were compared to their standard reference (Table 6). Using the Scherrer equation and the full width at half maximum (FWHM) from the XRD data, the crystal size of the reduced materials was determined. The results indicated that Ta-850-Mg-CL had a larger crystal size compared to Ta-Ap-Mg-CL. The difference in crystal size is attributed to the additional 850 °C thermal treatment in air performed to Ta-850 precursor prior to the Mg reduction procedure.

Table 6. X-ray diffraction parameters of Ta-Ap-Mg-CL and Ta-850-Mg-CL.

Sample	Peak (hkl)	Peak location (2θ)	d-spacing (\AA)	Lattice constant (\AA)	Crystal size (nm)
TaO standard reference	111	35.47	2.53	4.38	N/A
Ta-Ap-Mg-CL	111	34.78	2.58	4.46	2.70
Ta ₂ O standard reference	220	38.15	2.36	6.68	N/A
Ta-850-Mg-CL	220	37.34	2.41	6.80	11.91

The shift in peak position observed after reduction by Mg and chemical leaching led to a subsequent analysis of the peak location between experimental values and standard references. Figure 20 shows that the (111) plane of TaO standard reference was located at a 2θ value of 35.5°; however, the (111) plane in Ta-Ap-Mg sample was located at a 2θ value of 35.3°, and after chemical leaching it shifted further down to a 2θ value of 34.8°. The same trend was observed for the (220) plane of Ta₂O standard reference which

was located at a 2θ value of 38.2° , but the (220) plane location of Ta-850-Mg and Ta-850-Mg-CL were further down at 2θ values of 37.7° and 37.3° respectively.

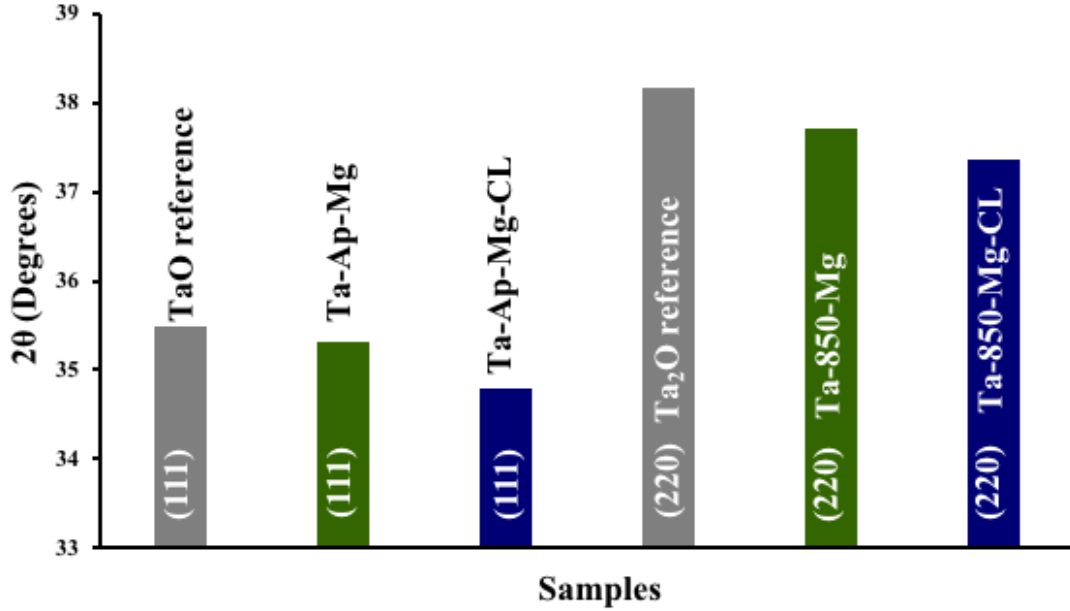


Figure 20. Average 2θ values for the (111) peak on TaO standard (gray), Ta-Ap-Mg (green), and Ta-Ap-Mg-CL (blue); average 2θ values for the (220) peak of Ta₂O standard (gray), Ta-850-Mg (green), and Ta-850-Mg-CL (blue).

Typically, it is known that a shift in peak position to lower theta values is attributed to a unit cell enlargement. A prior study has indicated that tantalum's unit cell constant is known to depend on the oxygen content in the metal according to Equation 14, where a is the Ta unit cell constant (\AA) and c_o is the oxygen content in the metal (at%).⁵⁹

$$a = 3.3030 + 0.0039 c_o \quad (14)$$

Furthermore, it has also been reported that the out-of-space lattice parameter and tetragonality increase with decreasing oxygen concentration, indicating that the crystal structure is closely related to the oxygen content.⁶⁹ As a result, a linear extrapolation analysis was used to estimate the oxygen content of the reduced samples in comparison to

their standard reference based on the d-spacing and stoichiometry obtained from the XRD analysis (Table 6).

The linear extrapolation was done with the assumption that the same crystal structure was maintained as the oxygen content increased, but this trend may not hold true for larger oxygen concentrations. The analysis was inspired by Vegard's law which indicates that a linear relationship exists between the crystal lattice constant of an alloy and the concentrations of the constituents elements.⁷⁰ Although the reduced TaO_x aerogels are not alloys and variables used in Vegard's law are not used, the shift to lower theta values of the reduced TaO_x aerogel materials is related to a unit cell enlargement which may be due to a higher oxygen content in the reduced samples compared to their standard references. Based on the previous assumptions, the d-spacing and final stoichiometry of Ta-Ap-Mg-CL and Ta-850-Mg-CL samples were compared to the d-spacing and stoichiometry of metallic Ta, TaO, and Ta₂O standard references.

The TaO standard reference had a d-spacing value of 2.53 Å for the (111) plane, and the stoichiometry was assumed to have a ratio of tantalum to oxygen of 1 to 1 with an oxygen concentration of 50%. The metallic-Ta had a d-spacing value of 2.44 Å for the (111) plane and it was assumed to have 0% of oxygen concentration. The experimental data of Ta-Ap-Mg-CL sample with a TaO crystal structure had a d-spacing value of 2.88 Å for the (111) plane. Based on the linear extrapolation, it was determined that Ta-Ap-Mg-CL sample had an oxygen concentration of 76 % indicating that it had 26% more of oxygen compared to the 50% observed on the standard reference of TaO (Figure 21).

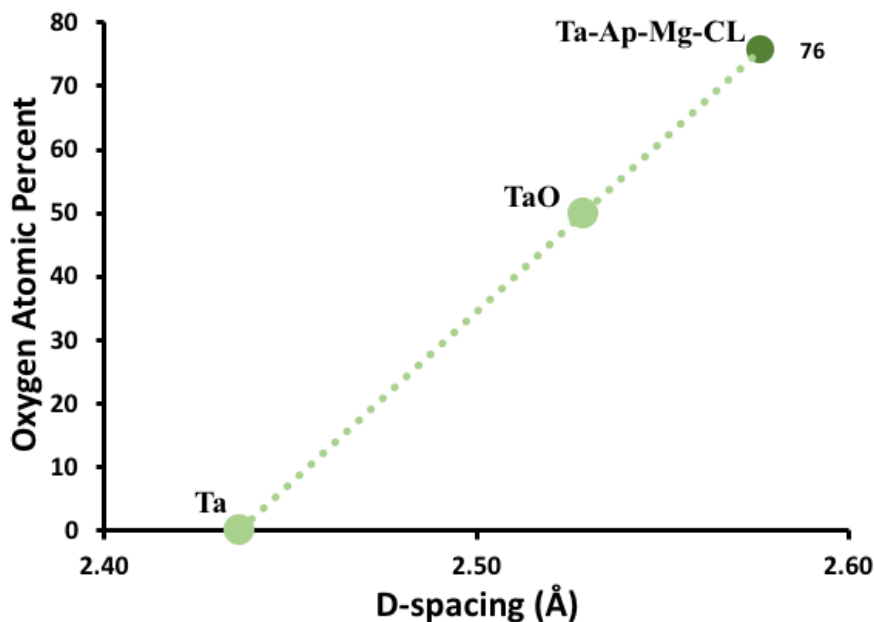


Figure 21. Linear extrapolation of the oxygen content in metallic Ta standard reference, TaO standard reference, and Ta-Ap-Mg-CL aerogel sample.

For the linear extrapolation of Ta-850-Mg-CL sample, the (220) plane was more adequate for comparison of the body-centered cubic Ta₂O crystal structure and the body-centered cubic metallic Ta. The Ta₂O standard reference had a d-spacing value of 2.36 Å for the (220) plane, and the stoichiometry was assumed to have a ratio of tantalum to oxygen of 2 to 1 with an oxygen concentration of 33 %. The metallic Ta standard reference had a d-spacing value of 1.17 Å for the (220) plane, and it was assumed to have 0% of oxygen concentration. The experimental data for the (220) plane of the Ta-850-Mg-CL sample with a Ta₂O crystal structure indicated a d-spacing value of 2.4 Å and the linear extrapolation determined an oxygen concentration of 35 %. The oxygen content in Ta-850-Ap-Mg is only 2% higher than the standard reference Ta₂O (Figure 22).

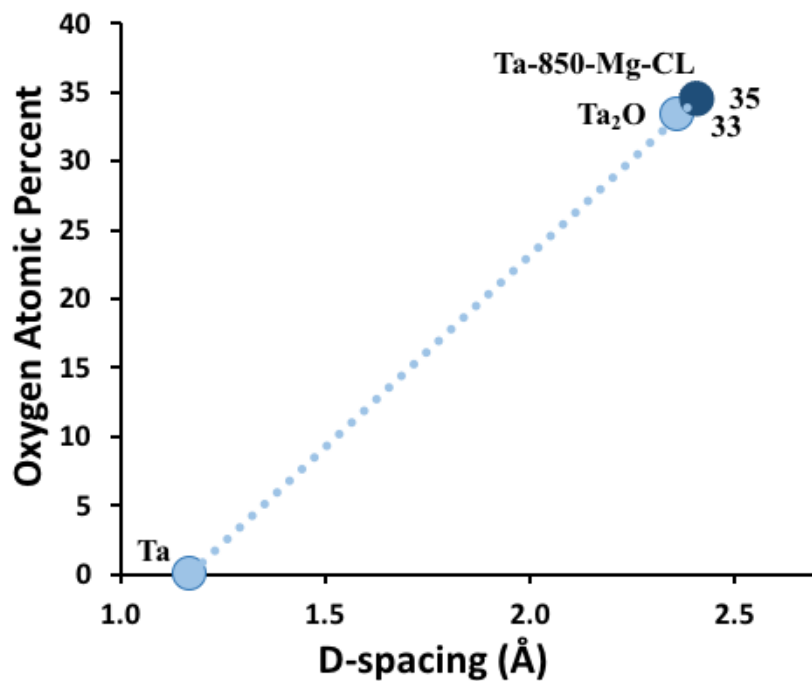


Figure 22. Linear extrapolation of the oxygen content in metallic Ta standard reference, Ta₂O standard reference, and Ta-850-Mg-CL aerogel sample.

The linear extrapolation analysis showed that both samples Ta-ap-Mg-CL and Ta-850-Mg-CL may have a higher oxygen content compared to their standard reference. It was observed that the chemical leaching step apart from removing MgO impurities, it was also oxidizing the reduced TaO_x materials. Overall, the higher oxygen content in the reduced samples agrees not only with the shift in peak position to lower theta values, but also with the larger unit cell determined for the reduced samples compared to their standard reference.

3.8 Comparison of The Composition from EDS and XRD Analysis

Table 7. Composition of TaO_x aerogels from Energy Dispersive X-ray Spectroscopy (EDS) and X-ray Diffraction (XRD) analysis.

Material	Stoichiometry based on EDS	Stoichiometry based on XRD
Ta-Ap	TaO _{3.9}	Unknown – amorphous structure
Ta-Ap-Mg-CL	TaO _{3.1}	TaO ₁
Ta-850	TaO _{3.3}	TaO _{2.5}
Ta-850-Mg-CL	TaO _{1.6}	TaO _{0.5}

A comparison between the stoichiometry obtained from the EDS and XRD analysis was conducted in order to observe the difference in oxygen concentration before and after the Mg reduction method with the goal to have a better understanding of the difference observed in the crystal structure of the reduced materials (Table 7).

The trend observed for Ta-850 precursor is that its stoichiometry obtained from the EDS analysis has a higher oxygen content of 3.9 compared to the one obtained from the XRD analysis of 2.5. The difference may be attributed to the presence of small impurities from the sample holder used during the EDS analysis as well as the low precision of the analysis. Although, the initial stoichiometry for Ta-Ap precursor is unknown by the XRD analysis, the EDS analysis predicted an oxygen content of 3.9, which is much higher than the one in Ta-850 precursor. This discrepancy may be due to the contribution of surface oxygen, hydroxyl, or water groups on the material. Ta-Ap is an as-prepared TaO_x aerogel but Ta-850 is a TaO_x aerogel that has gone through a thermal treatment resulting in the loss of surface impurities as observed on the TGA results.

The trend observed after the Mg reduction method is that Ta-850-Mg-CL product has a lower oxygen content compared to Ta-Ap-Mg-CL product. It is possible that the

surface oxygen from hydroxyl groups or water in Ta-Ap may have influenced its final degree of reduction. A prior study of the reduction of Ta₂O₅ powder with magnesium gas indicated that Mg reduction of tantalum oxide started from the powder's surface via magnesium gas which led to the formation of magnesium oxide on the surface.⁶⁰ As the reduction reaction proceeded, the oxygen component inside the particles was diffused out. Based on this study, it is predicted that the metallic Mg had to first react with oxygen impurities present on the surface of the Ta-Ap aerogel before reaching the oxygen within the structure. Due to oxygen impurities on the surface, Ta-Ap-Mg-CL may have achieved a lower degree of reduction compared to Ta-850-Mg-CL.

3.9 Analysis of Surface Area and Porosity

Nitrogen physisorption analysis of the Ta-Ap sample indicated an initial BET surface area of 197 m²g⁻¹ and a mean pore diameter of 11 nm (Table 8). After Mg reduction process, the surface area of Ta-Ap-Mg-CL and Ta-850-Mg-CL decreased to 54 m²g⁻¹ and 11 m²g⁻¹ respectively; however, the mean pore diameter for both products increased to 12 nm and 23 nm respectively. Apart from the effect of the thermal treatment during the Mg reduction method, the low surface area of Ta-850-Mg-CL is attributed to particle growth and coalescence promoted by the initial 850 °C thermal treatment performed prior to its reduction. Although the final surface area of the reduced TaO_x aerogel samples is low compared to the typical surface areas reported for carbon-based supports (100-1000 m²g⁻¹),⁹ the surface area of Ta-Ap-Mg-CL aerogel is in the range of surface areas previously reported for other metal oxide aerogels used as support materials (40 to 75 m²g⁻¹).^{15, 41-42}

Table 8. N₂ Physisorption surface area, cumulative pore volume, and mean pore diameter of materials: Ta-Ap, Ta-Ap-Mg-CL, and Ta-850-Mg-CL.

Material	Surface Area (m ² /g)	Cumulative Pore Volume (cm ³ /g)	Mean Pore Diameter (nm)
Ta-Ap	197	0.8	11
Ta-Ap-Mg-CL	54	0.2	12
Ta-850-Mg-CL	11	0.1	23

Apart from a high surface area, a catalyst support should possess a small percentage of micropores, a high percentage of mesopores, and some percentage of macropores. The pore size distribution analysis (Figure 23) showed that Ta-Ap had a small contribution of micropores (< 2 nm), a large contribution of mesopores (2-50 nm), and a small contribution of macropores (>50nm).

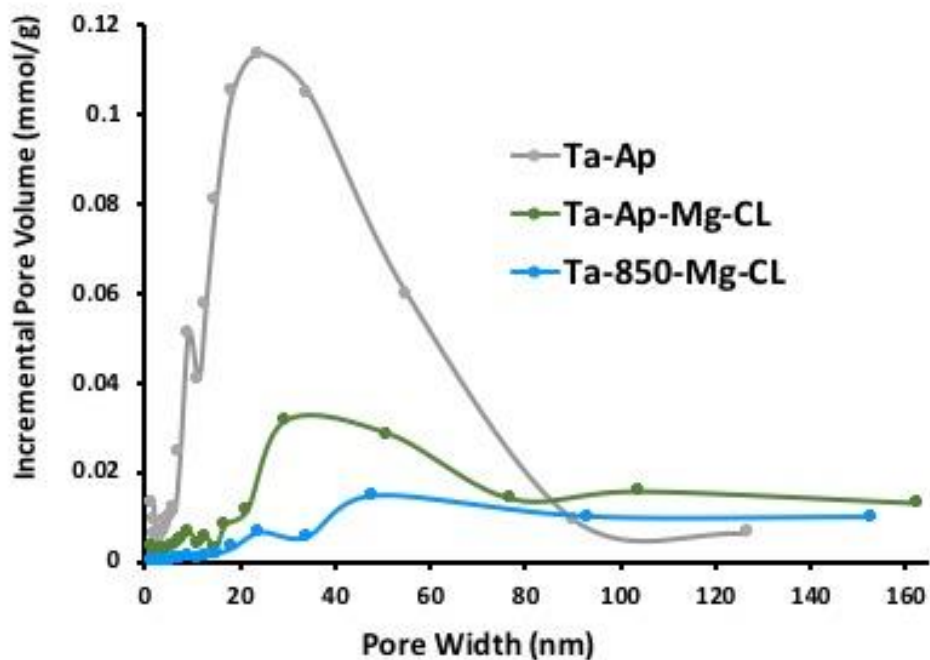


Figure 23. Pore size distribution of the as-prepared TaO_x aerogel (gray), Ta-Ap-Mg-CL (green), Ta-850-Mg-CL (blue).

After Mg reduction and chemical leaching, the pore size distribution indicated an increase in the average pore size. Both, Ta-Ap-Mg-CL and Ta-850-Mg-CL samples no

longer had a contribution of micropores, but mainly consisted of mesopores and a few macropores. Overall, the pore size distribution indicated that the reduction by Mg and the chemical leaching increased the pore size of Ta-Ap-Mg-CL and Ta-850-Mg-CL samples but decreased their cumulative pore volume.

3.10 Evaluation of The Electronic Conductivity

There are different factors that can influence the electronic conductivity of TaO_x aerogels including grain-boundary resistance, band gap, crystal structure, composition, pore size, and the measurement technique.

Table 9. Electronic conductivity of Ta-Ap, Ta-Ap-Mg-CL, and Ta-850-Mg-CL.

Sample	Electronic Conductivity Scm ⁻¹
Ta-Ap	3.5 x10 ⁻¹⁰
Ta-Ap-Mg-CL	3.7 x10 ⁻³
Ta-850-Mg-CL	3.5 x10 ⁻⁴

The electronic conductivity measured for Ta-Ap was 3.4 x10⁻¹⁰ S cm⁻¹ (Table 9), which supports that the material is highly electronically insulating. The low electronic conductivity was attributed to the aerogel's mesoporous structure particularly to the presence of grains boundaries. Grain boundaries generate potential barriers acting as trapping centers of electrons.⁷¹⁻⁷² When a material has grain boundaries, the electric current is affected because the electrons cannot easily travel as compared to a material without grain boundaries. Although the electronic conductivity of Ta-850 precursor (crystalline structure) was not measured, it is expected to be higher than Ta-Ap precursor (amorphous structure) because of the difference in crystal structure. Prior studies had

indicated that the band gap of an amorphous phase is slightly larger than equivalent compositions in the crystalline phase.⁶⁵ A higher band gap in an amorphous material could lead to lower electronic conductivities. The calculated band gap for a crystalline Ta₂O₅ material was reported to be lower 4.03 eV than the calculated band gap for Ta₂O₅ amorphous material 4.52 eV.⁶⁶ Experimental studies have also shown a higher electronic conductivity for crystalline Ta ($1.1 \times 10^5 \text{ S cm}^{-1}$) compared to amorphous Ta ($8.7 \times 10^3 \text{ S cm}^{-1}$).⁶⁵ It suggested that due to the 850 °C thermal treatment and phase transformation from amorphous to crystalline Ta₂O₅ structure, Ta-850 precursor would have a higher electronic conductivity compared to Ta-Ap precursor.

Preliminary results indicated that the electronic conductivity of both Ta-Ap-Mg-CL and Ta-850-Mg-CL samples significantly improved after the reduction of TaO_x aerogels by Mg acting as a reducing agent. The increase in conductivity can be attributed to the change in oxygen composition. A prior study indicated that the electronic conductivity of TaO_x materials increased as the oxygen content in the crystal structure decreased ($\text{Ta}_2\text{O}_5 = 2 \times 10^{-9} \text{ S cm}^{-1} < \text{TaO} < \text{Ta}_2\text{O} = 6 \times 10^2 \text{ S cm}^{-1}$).⁶⁵ Furthermore, a study indicated that the conduction mechanism of tantalum was dependent upon its oxidation state.⁷³ Initially, Ta metal has a fine metallic conductivity, but once the oxidation state of Ta increases (Ta = lowest oxidation state < Ta₂O < TaO < Ta₂O₅ = highest oxidation state), the metallic conductivity changes to an electron hopping mechanism and ultimately the conductivity becomes very low due to the high resistivity. Since the final crystal structure of Ta-Ap-Mg-CL (TaO) and Ta-850-Mg-CL (Ta₂O) are oxygen deficient phases of tantalum pentoxide (Ta₂O₅), their higher electronic conductivity compared to Ta-Ap precursor is attributed to the lower oxygen content of these crystal structures.

Since Ta-850-Mg-CL reached a higher degree of reduction, less oxygen content, compared to Ta-Ap-Mg-CL, it was expected that it would have a higher electronic conductivity, but the experimental results indicated the opposite. This anomaly observed for Ta-Ap-Mg-CL was associated to the higher carbon content within the sample observed in the EDS analysis (Table 4). The presence of carbon has been directly correlated with an increased in the electronic conductivity of a material.⁷⁴ Based on the N₂ physisorption analysis (Table 8 & Figure 23), both reduced materials increased their pore size compared to the precursor. A prior study has also shown that the overall rate constant during charge transfer increased by a factor of 10 when the pore size tripled (1.5 nm to 4.7 nm), suggesting that pore size can improve the charge transfer efficiency.⁷⁵ For this reason, the increase in pore size of the reduced materials was also considered as a factor that may have enhanced their electronic conductivity.

Lastly, although several variables were controlled and different techniques were implemented to obtain reproducible results, a consistent and reliable method has not been developed to measure the electronic conductivities of reduced TaO_x aerogels. For this reason, this research project recognizes that these are preliminary results of single measurements of the reduced materials and acknowledges that the measuring technique and equipment are also factors that can affect the electronic conductivity.

In general there are different factors that affect the electronic conductivity of materials including grain-boundary resistance, band gap, crystal structure, composition, pore size, and measurement technique. Because preliminary results indicated an increase in the electronic conductivity of Ta-Ap-Mg-CL and Ta-850-Mg-CL samples, it is

suggested that reduction of TaO_x aerogels by Mg was a promising approach to enhance their electronic conductivity.

4. CONCLUSIONS

The motivation of this project was to develop TaO_x aerogels that could serve as potential carbon-free support materials for the ORR in PEMFC. The initial hypothesis tentatively predicted that Mg reduction will increase the electronic conductivity of TaO_x aerogels while retaining the properties of large surface area and porous morphology. Results indicated that via the sol-gel synthesis method, high surface area and porous TaO_x aerogels were successfully synthesized. Furthermore, TaO_x aerogels were able to retain an adequate porous morphology even after Mg reduction and chemical leaching. Although the final surface area of the TaO_x aerogels decreased as a result of thermal treatments and reduction conditions, the final surface area of the Ta-Ap-Mg-CL material was still adequate when it was compared to previously reported surface areas for other metal oxide supports.

The analysis on the effect of Mg reduction on the crystal structure of the TaO_x aerogel showed that the crystallinity of the precursor plays an important role in the degree of reduction of the final material. In performing Mg reduction on two different structures, amorphous (Ta-Ap) and crystalline (Ta-850), it was observed that Ta-Ap had a phase transition from amorphous to TaO crystal structure while Ta-850 had a phase transformation from monoclinic Ta₂O₅ to Ta₂O crystal structure. Ta-850 precursor reached a higher degree of reduction compared to Ta-Ap precursor, indicating that a crystalline precursor will reach a higher degree of reduction compared to an amorphous one. Analysis of XRD peak position indicated that both Ta-Ap-Mg-CL and Ta-850-Mg-CL had a higher content of oxygen compared to their standard references. In addition,

chemical leaching was found to not only remove MgO but also shift the XRD peaks position by adding oxygen to the structure.

Lastly, preliminary measurements of the electronic conductivity of TaO_x aerogels indicated that Mg reduction was a successful approach to increase the electronic conductivity of the materials. While the precursor (Ta-Ap) material had an electronic conductivity of $3.4 \times 10^{-10} \text{ S cm}^{-1}$, the reduced samples (Ta-Ap-Mg-CL and Ta-850-Mg-CL) had a higher electronic conductivity of $3.7 \times 10^{-3} \text{ S cm}^{-1}$ and $3.5 \times 10^{-4} \text{ S cm}^{-1}$ respectively. Hence Mg reduction was strong enough to reduce a highly stable and inert material such as TaO_x. Since the final electronic conductivity of the reduced samples were still low ($10^{-3} - 10^{-4} \text{ S cm}^{-1}$) compared to the typical electronic conductivities observed for carbon-based supports (1-10 S/cm), the processing conditions of Mg reduction on TaO_x aerogels should be improved.

Further studies are needed to (i) optimize the Mg reduction process (amount of Mg, temperature, and time of thermal treatment) to increase the electronic conductivity of TaO_x aerogels; (ii) improve the method used to measure the electronic conductivity of the reduced materials; and (iii) test the activity and stability of reduced Ta-based aerogels as electrocatalyst supports.

BIBLIOGRAPHY

1. MacKay, D. J., Solar Energy in the Context of Energy Use, Energy Transportation and Energy Storage. *Philosophical Transactions Of The Royal Society* **2013**, 371 (1996).
2. Ginley, D. S.; Cohen, D., Fundamentals of Materials for Energy and Environmental Sustainability. *Cambridge University Press*, **2012**.
3. Administration, U. S. E. I. A., U.S. Primary Energy Consumption by Energy Source. <https://www.eia.gov/energyexplained/us-energy-facts/>.
4. Layton, B. E., A Comparison of Energy Densities of Prevalent Energy Sources in Units of Joules Per Cubic Meter. *International Journal of Green Energy* **2008**, 5 (6), 438-455.
5. Sharaf, O. Z.; Orhan, M. F., An Overview of Fuel Cell Technology: Fundamentals and Applications. *Renewable and Sustainable Energy Reviews* **2014**, 32, 810-853.
6. Matthey, J., The Fuel Cell Today Industry Review 2011. *Fuel Cell Today, The Leading Authority on Fuel Cells* **2011**.
7. Wang, Y. J.; Wilkinson, D. P.; Zhang, J., Noncarbon Support Materials for Polymer Electrolyte Membrane Fuel Cell Electrocatalysts. *Chem Rev* **2011**, 111 (12), 7625-51.
8. Kreitmeier, S.; Wokaun, A.; Büchi, F, Local Catalyst Support Degradation During Polymer Electrolyte Fuel Cell Start-Up and Shutdown. *Journal of The Electrochemical Society* **2012**, 159 (11), F787-F793.
9. Büchi, F.; Inaba, M.; Schmidt, T., Polymer Electrolyte Fuel Cell Durability. *Springer* 2009.
10. Ren, P.; Pucheng, P.; Li, Y.; Wu, Z.; Chen, D.; Huang, S., Degradation Mechanisms of Proton Exchange Membrane Fuel Cell Under Typical Automotive Operating Conditions. *Progress in Energy and Combustion Science* **2020**, 80.
11. Meier, J.; Galeano, C.; Katsounaros, I.; Witte, J.; Bongard, H. J.; Topalov, A. A.; Baldizzone, C.; Mezzavilla, S.; Schuth, F.; Mayrhofer, K. J. J., Design Criteria for Stable Pt/C Fuel Cell Catalysts. *Beilstein Journal of Nanotechnology* **2014**, 5, 44-67.
12. Zhang, Z.; Liu, J.; Gu, J.; Su, L.; Cheng, L., An Overview of Metal Oxide Materials as Electrocatalysts and Supports for Polymer Electrolyte Fuel Cells. *Energy Environ. Sci.* **2014**, 7 (8), 2535-2558.

13. Hoogers, G., Fuel Cell Technology Handbook *CRC Press LLC*: 2003.
14. Rolison, D., Catalytic Nanoarchitectures-The Importance of Nothing and The Unimportance of Periodicity. *Science* **2003**, *299*, 1698-1701.
15. Beauger, C.; Testut, L.; Berthon-Fabry, S.; Georgi, F.; Guetaz, L., Doped TiO₂ Aerogels as Alternative Catalyst Supports for Proton Exchange Membrane Fuel Cells: A Comparative Study of Nb, V and Ta Dopants. *Microporous and Mesoporous Materials* **2016**, *232*, 109-118.
16. Levy, N.; Lori, O.; Gonen, S.; Mizrahi, M.; Ruthstein, S.; Elbaz, L., The Relationship of Morphology and Catalytic Activity: A Case Study of Iron Corrole Incorporated in High Surface Area Carbon Supports. *Carbon* **2020**, *158*, 238-243.
17. Stoerzinger, K. A.; Choi, W. S.; Jeon, H.; Lee, H. N.; Shao-Horn, Y., Role of Strain and Conductivity in Oxygen Electrocatalysis on LaCoO₃ Thin Films. *The Journal of Physical Chemistry Letters* **2015**, *6* (3), 487-92.
18. Chung, D.; Yoo, J. M.; Sung, Y. E., Highly Durable and Active Pt-Based Nanoscale Design for Fuel-Cell Oxygen-Reduction Electrocatalysts. *Advanced Materials* **2018**, *30* (42), 1704123(1)-1704123(20).
19. Ho, V. T.; Pan, J.; Rick, J.; Su, W. N.; Hwang, B. J., Nanostructured Ti_{0.7}Mo_{0.3}O₂ Support Enhances Electron Transfer to Pt: High-Performance Catalyst for Oxygen Reduction Reaction. *Journal of the American Chemical Society* **2011**, *133* (30), 11716-11724.
20. Kumar, A.; Ramani, V., Strong Metal–Support Interactions Enhance the Activity and Durability of Platinum Supported on Tantalum-Modified Titanium Dioxide Electrocatalysts. *ACS Catalysis* **2014**, *4* (5), 1516-1525.
21. Pan, C.; Tsai, M.; Su, W.; Rick, J.; Akalework, N.; Agegnehu, A.; Cheng, S.; Hwang, B., Tuning/Exploiting Strong Metal-Support Interaction (SMSI) in Heterogeneous Catalysis. *Journal of the Taiwan Institute of Chemical Engineers* **2017**, *74*, 154-186.
22. Gao, W.; Zhengping, Z.; Dou, M.; Wang, F., Highly Dispersed and Crystalline Ta₂O₅ Anchored Pt Electrocatalyst with Improved Activity and Durability Toward Oxygen Reduction: Promotion by Atomic-Scale Pt–Ta₂O₅ Interactions. *ACS Catalysis* **2019**, *9* (4), 3278-3288.
23. Sasaki, K.; Fumiaki, T.; Noda, Z.; Hayashi, S.; Shiratori, Y.; Ito, K., Alternative Electrocatalyst Support Materials for Polymer Electrolyte Fuel Cells. *The Electrochemical Society* **2010**, *33* (1), 473-482.

24. Kumar, A.; Ramani, V., Ta_{0.3}Ti_{0.7}O₂ Electrocatalyst Supports Exhibit Exceptional Electrochemical Stability. *Journal of The Electrochemical Society* **2013**, *160* (11), F1207-F1215.
25. Ioroi, T.; Siroma, Z.; Fujiwara, N.; Yamazaki, S.; Yasuda, K., Sub-Stoichiometric Titanium Oxide-Supported Platinum Electrocatalyst for Polymer Electrolyte Fuel Cells. *Electrochemistry Communications* **2005**, *7*, 183-188.
26. Huang, S.; Ganesan, P.; Park, S.; Popov, B., Development of a Titanium Dioxide-Supported Platinum Catalyst with Ultrahigh Stability for Polymer Electrolyte Membrane Fuel Cell Applications. *Journal of the American Chemical Society* **2009**, *131* (39), 13898-13899.
27. Zhang, J.; Coms, F.D.; Kumaraguru, S. Necessity to Avoid Titanium Oxide As Catalyst Support in PEM Fuel Cells. *General Motors Company: 235th Electrochemical Society Meeting*, 2019; p 2.
28. Tripković, V.; Abild-Pedersen, F.; Studt, F.; Cerri, I.; Nagami, T.; Bligaard, T.; Rossmeisl, J., Metal Oxide-Supported Platinum Overlayers as Proton-Exchange Membrane Fuel Cell Cathodes. *ChemCatChem* **2012**, *4* (2), 228-235.
29. Veazey, W. R., *CRC Handbook of Chemistry and Physics*. 100th ed.; United States of America, 2019.
30. Pourbaix, M., *Atlas of Electrochemical Equilibria in Aqueous Solutions*. NACE International Cebelcor: 1974; p 1-648.
31. TANTALINE The Corrosion Resistance of Tantalum.
<https://tantaline.com/technology/corrosion-properties/>.
32. Awaludin, Z.; Moo, J.G.; Okajima, T.; Ohsaka, T., TaO_x-Capped Pt Nanoparticles as Active and Durable Electrocatalysts for Oxygen Reduction. *Journal of Materials Chemistry A* **2013**, *1* (46), 14754-14765.
33. Awaludin, Z.; S.usuki, M.; Masud, J.; Okajima, T.; Ohsaka, T., Enhanced Electrocatalysis of Oxygen Reduction on Pt/TaO_x/GC. *The Journal of Physical Chemistry C* **2011**, *115* (51), 25557-25567.
34. D'Urso, C.; Bonura, G.; Aricò, A. S., Synthesis and Physical-Chemical Characterization of Nanocrystalline Ta modified TiO₂ as Potential Support of Electrocatalysts for Fuel Cells and Electrolyzers. *International Journal of Hydrogen Energy* **2017**, *42* (46), 28011-28021.

35. Song, Z.; Banis, M.; Zhang, L.; Wang, B.; Yang, L.; Banham, D.; Zhao, Y.; Liang, J.; Zheng, M.; Li, R.; Ye, S.; Sun, X., Origin of Achieving the Enhanced Activity and Stability of Pt Electrocatalysts with Strong Metal-Support Interactions Via Atomic Layer Deposition. *Nano Energy* **2018**, *53*, 716-725.
36. Anwar, M. T.; Yan, X.; Shen, S.; Husnain, N.; Zhu, F.; Luo, L.; Zhang, J., Enhanced Durability of Pt Electrocatalyst with Tantalum Doped Titania as Catalyst Support. *International Journal of Hydrogen Energy* **2017**, *42* (52), 30750-30759.
37. Flannery, L.; Nimens, W.; Rahman, Aj.; Whittaker-Brooks, L., WWMOD? What Would Metal Oxides Do?: Redefining Their Applicability in Today's Energy Technologies. *Polyhedron* **2019**, *170*, 334-358.
38. Sahin, I.; Inonu, Z.; Ulker, Z.; Erkey, C., Kinetics of Supercritical Drying of Gels. *Gels* **2017**, *4* (1).
39. Rolison, D.; Dunn, B., Electrically Conductive Oxide Aerogels: New Materials in Electrochemistry. *Journal of Materials Chemistry* **2001**, *11* (4), 963-980.
40. García-González, C.; Camino-Rey, M.; Alnaief, M.; Zetzl, C.; Smirnova, I., Supercritical Drying of Aerogels Using CO₂: Effect of Extraction Time on the End Material Textural Properties. *The Journal of Supercritical Fluids* **2012**, *66*, 297-306.
41. Ozouf, G.; Beauger, C., Niobium- and Antimony-Doped Tin Dioxide Aerogels as New Catalyst Supports for PEM Fuel Cells. *Journal of Materials Science* **2016**, *51* (11), 5305-5320.
42. Solà-Hernández, L.; Claudel, F.; Maillard, F.; Beauger, C., Doped Tin Oxide Aerogels as Oxygen Evolution Reaction Catalyst Supports. *International Journal of Hydrogen Energy* **2019**, *44* (45), 24331-24341.
43. Maurer, S. M.; Ko, E., Structural and Acidic Characterization of Niobia Aerogels. *Journal of Catalysis* **1992**, *135*, 125-134.
44. Stöcker, C.; Baiker, A., Zirconia Aerogels: Effect of Acid-to-Alkoxide Ratio, Alcoholic Solvent and Supercritical Drying Method on Structural Properties. *Journal of Non-Crystalline Solids* **1998**, *223*, 165-178.
45. Pan, L.; Huang, H.; Liu, T.; Niederberger, M., Structurally Disordered Ta₂O₅ Aerogel for High-Rate and Highly Stable Li-ion and Na-ion Storage Through Surface Redox Pseudocapacitance. *Electrochimica Acta* **2019**, *321*.
46. Ren, H.; Zhang, L.; Shang, C.; Wang, X.; Bi, Y., Synthesis of a Low-Density Tantalum Oxide Tile-Like Aerogel Monolithic. *Journal of Sol-Gel Science and Technology* **2010**, *53* (2), 307-311.

47. Sasaki, K.; Takasaki, F.; Noda, Z.; Hayashi, S.; Shiratori, Y.; Ito, K., Alternative Electrocatalyst Support Materials for Polymer Electrolyte Fuel Cells. *The Electrochemical Society* **2010**, *33* (1), 473-482.
48. Takabatake, Y.; Noda, Z.; Lyth, S.; Hayashi, A.; Sasaki, K., Cycle Durability of Metal Oxide Supports for PEFC Electrocatalysts. *International Journal of Hydrogen Energy* **2014**, *39* (10), 5074-5082.
49. Chhina, H.; Campbell, S.; Kesler, O., Ex Situ and In Situ Stability of Platinum Supported on Niobium-Doped Titania for PEMFCs. *Journal of The Electrochemical Society* **2009**, *156* (10), B1232-B1237.
50. Sasaki, K.; Zhang, L.; Adzic, R., Niobium Oxide-Supported Platinum Ultra-Low Amount Electrocatalysts for Oxygen Reduction. *Phys Chem Chem Phys* **2008**, *10* (1), 159-67.
51. Ambreen, S.; Pandey, N.; Mayer, P.; Pandey, A., Characterization and Photocatalytic Study of Tantalum Oxide Nanoparticles Prepared by the Hydrolysis of Tantalum Oxo-ethoxide $Ta_8(3\mu-O)_2(\mu-O)_8(\mu-OEt)_6(OEt)_{14}$. *Beilstein Journal of Nanotechnology* **2014**, *5*, 1082-1090.
52. Chun W.; Ishikawa, A.; Fujisawa, H.; Takata, T.; Kondo, J.N.; Hara, M.; Kawai, M.; Matsumoto, Y.; Domen, K., Conduction and Valence Band Positions of Ta_2O_5 , $TaON$, and Ta_3N_5 by UPS and Electrochemical Methods. *The Journal of Physical Chemistry B* **2003**, *107* (8), 1798-1803.
53. Bondi, R. J.; Desjarlais, M. P.; Thompson, A. P.; Brennecke, G. L.; Marinella, M. J., Electrical Conductivity in Oxygen-Deficient Phases of Tantalum Pentoxide From First-Principles Calculations. *Journal of Applied Physics* **2013**, *114* (20).
54. Lee, N.; Yoon, K.; Lee, J.; Park, Y.; Pyo, S.; Kim, G.; Ha, D.; Ryu, W., Highly Conductive Off-Stoichiometric Zirconium Oxide Nanofibers with Controllable Crystalline Structures and Bandgaps and Improved Electrochemical Activities. *ACS Applied Energy Materials* **2019**, *2* (5), 3513-3522.
55. Strunk, J.; Vining, W.; Bell, A., A Study of Oxygen Vacancy Formation and Annihilation in Submonolayer Coverages of TiO_2 Dispersed on MCM-48. *The Journal of Physical Chemistry C* **2010**, *114* (40), 16937-16945.
56. Dissanayake, L., Nano-Composite Solid Polymer Electrolytes for Solid State Ionic Devices. *Ionics* **2004**, *10*, 221-225.
57. Yang, T.; Liu, Y.; Zhang, M., Improving the Electrochemical Properties of $Cr-SnO_2$ by Multi-Protecting Method Using Graphene and Carbon-Coating. *Solid State Ionics* **2017**, *308*, 1-7.

58. Orlov, V.; Kryzhanov, M., Magnesium-Thermic Reduction of Tantalum Oxide by Self-Propagating High-Temperature Synthesis. *Russian Metallurgy (Metally)* **2010**, (5), 384-388.
59. Orlov, V.; Kryzhanov, M.; Kalinnikov, V. T., Magnesium Reduction of Tantalum Oxide Compounds. *Doklady Chemistry* **2014**, 457 (2), 160-163.
60. Hwang, S.; Wang, J.; Lee, D., Extraction of Tantalum Powder via the Magnesium Reduction of Tantalum Pentoxide. *Metals* **2019**, 9 (205).
61. Xia, Y.; Fang, Z.; Zhang, Y.; Lefler, H.; Zhang, T.; Sun, P.; Huang, Z., Hydrogen Assisted Magnesiothermic Reduction (HAMR) of Commercial TiO₂ to Produce Titanium Powder with Controlled Morphology and Particle Size. *Materials Transactions* **2017**, 58 (3), 355-360.
62. Gourishankar, K. V.; Ranjbar, M.K.; Pierre, G.R. , Revision of the Enthalpies and Gibbs Energies of Formation of Calcium Oxide and Magnesium Oxide. *Journal of Phase Equilibria* **1993**, 14 (5), 601-611.
63. Jacob, K. T.; Rajput, A., Phase Relations in the System Ca-Ta-O and Thermodynamics of Calcium Tantalates in Relation to Calciothermic Reduction of Ta₂O₅. *Journal of Alloys and Compounds* **2015**, 620, 256-262.
64. Ye, M.; Jia, J.; Wu, Z.; Qian, C.; Chen, R.; O'Brien, P.; Sun, W.; Dong, Y.; Ozin, G., Synthesis of Black TiO_x Nanoparticles by Mg Reduction of TiO₂ Nanocrystals and Their Application for Solar Water Evaporation. *Advanced Energy Materials* **2017**, 7 (4).
65. Bondi, R. J.; Desjarlais, M. P.; Thompson, A. P.; Brennecka, G. L.; Marinella, M. J., Electrical Conductivity in Oxygen-Deficient Phases of Tantalum Pentoxide from First-Principles Calculations. *Journal of Applied Physics* **2013**, 114 (20), 203701-1 - 203701-16.
66. Guo, Y.; Robertson, J., Comparison of Oxygen Vacancy Defects in Crystalline and Amorphous Ta₂O₅. *Microelectronic Engineering* **2015**, 147, 254-259.
67. Cox, D. F.; Fryberger, T. B.; Semancik, S., Oxygen Vacancies and Defect Electronic States on the SnO₂(110)-1x1 Surface. *Phys Review B* **1988**, 38 (3), 2072-2083.
68. *Transition Metal Oxides Surface Chemistry and Catalysis*. 1989; Vol. 45, p 91-109.
69. Enriquez, E.; Chen, A.; Harrell, Z.; Dowden, P.; Koskelo, N.; Roback, J.; Janoschek, M.; Chen, C.; Jia, Q., Oxygen Vacancy-Tuned Physical Properties in Perovskite Thin Films with Multiple B-site Valance States. *Scientific Reports* **2017**, 7, 46184(1)-46184(8).

70. Denton, A. R.; Ashcroft, N. W., Vegard's Law. *Physical Review A* **1991**, *43* (6), 3161-3164.
71. Matsui, H.; Tabat, H., Correlation of Self-Organized Surface Nanostructures and Anisotropic Electron Transport in Nonpolar ZnO (10–10) Homoepitaxy. *Journal of Applied Physics* **2006**, *99* (12).
72. Salzman, J.; Uzan-Saguy, C.; Meyler, B.; Kalish, R., The Effect of Grain Boundaries on Electrical Conductivity in Thin GaN Layers. *Physica Status Solidi* **1999**, *176*, 683-687.
73. Goldfarb, I.; Miao, F.; Yang, J.; Yi, W.; Strachan, J. P.; Zhang, M. X.; Pickett, M. D.; Medeiros-Ribeiro, G.; Williams, R. Stanley, Electronic Structure and Transport Measurements of Amorphous Transition-Metal Oxides: Observation of Fermi Glass Behavior. *Applied Physics A Materials Science & Processing* **2012**, *107*, 1-11.
74. Wiora, N.; Mertens, M.; Brühne, K.; Fecht, H.; Tran, I.; Willey, T.; Van Buuren, A.; Biener, J.; Lee, J., Grain Boundary Dominated Electrical Conductivity in Ultrananocrystalline Diamond. *Journal of Applied Physics* **2017**, *122* (14).
75. Cai, M.; Loague, Q.; Morris, A. J., Design Rules for Efficient Charge Transfer in Metal-Organic Framework Films: The Pore Size Effect. *The Journal Physical Chemistry Letters* **2020**, *11* (3), 702-709.